Indoor RIS-Assisted Wireless System with Location-Based Reflective Patterns

Yuan, Jide; Franek, Ondrej; Fang, He; Popovski, Petar

Published in:
IEEE Transactions on Communications

DOI (link to publication from Publisher):
10.1109/TCOMM.2024.3402617

Publication date:
2024

Document Version
Accepted author manuscript, peer reviewed version

Indoor RIS-Assisted Wireless System with Location-Based Reflective Patterns

Jide Yuan, *Member, IEEE*, Ondrej Franek, *Member, IEEE*, He Fang, *Member, IEEE*, and Petar Popovski, *Fellow, IEEE*

***Abstract*—Reconfigurable intelligent surface (RIS) has emerged as a highly promising infrastructure benefiting from its capability to manipulate the propagation environment and facilitate efficient aggregation of wireless transmission signals. However, a major challenge in these systems is the significant overhead incurred by the acquisition of channel state information. This paper proposes a pre-designed beam-based transmission protocol that aims to reduce the burden of pilot overhead by designing a RIS reflective pattern codebook as an alternative to channel estimation (CE). We adopt an electromagnetic-compliant RIS model and develop a theoretical approximate expression for the channel gain, incorporating the impact of location mismatch. This approximation facilitates the construction of a location-based reflective pattern codebook, wherein the chosen locations linked with the codewords represent optimal location sampling points derived from theoretical results. By utilizing the constructed codebook, our proposed transmission protocol enables the system to search reflective patterns instead of real-time optimization. To validate our approach, extensive numerical simulations are conducted. The results demonstrate the accuracy of the approximate channel gain expression and highlight the superior coverage achieved by the proposed location-based reflective pattern codebook as well as the achievable spectral efficiency of our transmission protocol.**

***Index Terms*—Achievable spectral efficiency, channel gain, coverage, reconfigurable intelligent surface, transmission protocol**

I. Introduction

The continuous demand for faster, lower latency, and more reliable communication systems in the context of B5G/6G networks has led to the exploration of novel technologies to address the challenges posed by complex, diverse, and ubiquitous dense communication scenarios. However, advancements in physical layer technologies for sources and hosts have nearly exhausted the available time and frequency resources, making it crucial to explore alternative approaches to enhance system performance. In this regard, reconfigurable intelligent surfaces (RIS) have attracted significant attention and research interest from academia and industry due to their ability to modify the propagation environment [1]. The ability of RIS to manipulate the propagation environment comes from the large number of passive reflective units integrated on its surface. These reflective units are controlled by a field programmable gate array (FPGA) and have the ability to modify the frequency, phase, or amplitude of the incident signal by adjusting the capacitance or conductance within the unit [2, 3]. A key aspect contributing to the enhancement of achievable spectral efficiency (SE) in RIS lies in its ability to adjust the phase of the incident signal across each reflective unit which helps to mitigate the small-scale fading resulting from signal coherence, thus acting as a passive beamformer [4, 5].

RIS presents a wide range of research prospects and challenges across various domains, including hardware design [6, 7], RIS modeling [8, 9], performance evaluation [9, 10], RIS optimization [11], transmission protocol design [12], and compatibility validation [13, 14]. The existing literature on RIS can be broadly categorized into three perspectives. The *first* perspective focuses on studying the electromagnetic and radiation characteristics of RIS by considering hardware design and constructing RIS models to uncover its constraints and limitations. The path-loss model and mutual coupling are experimentally verified in [8] and [15], respectively. In [16], a prototype of RIS is presented where the reflection properties are controlled by four voltage-controlled varactors. It is characterized that the RIS can achieve an omnidirectional reflective pattern with equal gain only when the incident signal angles are within the range of $\pm 40^{\circ}$.

The *second* perspective involves the application of RIS to localization and sensing. Such a system can harness the additional communication links provided by RIS to enhance spatial sensing capabilities while simplifying optimization problems in communication through acquired user location data from the RIS. In [17], the joint sensing and access problem is investigated from the perspective of the MAC layer. In indoor scenarios, the system constructs a channel oracle that incorporates knowledge of location-based channel variations associated with RIS reflective patterns. This enables the system to tailor access policies for individual UEs based on their locations and to utilize RIS as a mediator to implement time-division multiple access (TDMA). In the *third* perspective, researchers investigate the potential benefits of integrating RIS into communication systems from a communication perspective. The

Manuscript received October 23, 2023; revised March 19, 2024, and April 29, 2024; accepted May 9, 2024. This work was supported in part by the National Science Fund for Distinguished Young Scholars 62301350, the Natural Science Foundation of the Jiangsu Higher Education Institutions of China with Grant 23KJB510027, the EU H2020 project RISE-6G, and the Villum Investigator Grant "WATER" from the Velux Foundation, Denmark. The associate editor coordinating the review of this paper and approving it for publication was M. Elkashlan.

Jide Yuan is with the School of Electronic and Information Engineering, Soochow University, Suzhou 215006, P. R. China (e-mail: yuanjide@suda.edu.cn).

Ondrej Franek is with the Department of Radio Electronics, Brno University of Technology, 601 90 Brno, Czech Republic (e-mail: of@es.aau.dk).

He Fang is with the College of Computer and Cyber Security, Fujian Normal University, Fujian 350117, P. R. China (e-mail: fanghe@fjnu.edu.cn).

Petar Popovski is with the Connectivity Section, Department of Electronic Systems, Aalborg University, Denmark. (e-mail: petarp@es.aau.dk).

objective is to evaluate and optimize the system performance in areas such as RIS-assisted multiple-input multiple-output (MIMO) [18, 19], cell-edge enhancement [20, 21], and RIS-assisted integrated sensing, communication (ISAC) [22–24], among others. For instance, Björnson *et al.* [25] compare RIS-aided systems with decode-and-forward relaying systems, assuming an ideal phase-shifting reflective pattern. In [12], RIS is utilized in an orthogonal-frequency division multiplexing (OFDM) system, and the reflective units are optimized in a group-wise fashion to improve the quality of service for cell-edge users. In [26], a passive beamforming optimization considering hardware impairments is proposed, revealing a significant performance gap compared to the conventional ideal phase-shifting RIS in single-user and multiuser scenarios. However, it is important to highlight that the performance improvement offered by RIS relies on the accurate estimation of channel state information (CSI) for each reflective unit, making CSI acquisition for AP-RIS-user links a key challenge.

The passive nature of RIS poses practical challenges in channel estimation (CE), as the reflective paths are coupled at the receiver. To estimate individual reflective channels, a significant number of pilots is required to decouple these paths. Mathematically, it necessitates N (the number of reflective units on RIS) times the pilot overhead of conventional communication systems, which is unaffordable [27, 28]. While some research has proposed overhead-efficient estimation algorithms for spatial sparse channels, it is important to note that these algorithms are primarily designed for far-field MISO/SIMO systems and may not readily extend to near-field scenario or MIMO systems due to their specific pre-processing requirements [29–31]. Due to the challenges associated with channel acquisition, RIS holds greater promise in indoor communication scenarios characterized by stable propagation environments [32–34]. The scatter locations remain fixed in indoor settings, leading to relatively stable channel characteristics across the room. This stability allows for the utilization of historical channel information, enabling the optimal configuration of the RIS and reducing the reliance on real-time channel estimation. There has been a variety of studies investigating the indoor RIS-assisted system. For example, [35] discussed passive RIS and active RIS within the context of power budget constraints, highlighting the tradeoffs and feasibility of active RIS. The upper bound on outage probability has been analyzed in the presence of location uncertainty in an indoor scenario [36]. This analysis provides an effective method to simplify power optimization problems in RIS-assisted systems. The authors further integrated RIS into the existing OFDM system, leveraging location information for resource allocation instead of relying on real-time CSI [37]. The authors of [38, 39] proposed a two-timescale optimization approach for RIS-assisted systems, where passive and active beamforming rely on long-term CSI and instantaneous CSI, respectively. The hardware impairment has been considered in [40], where a joint beamforming optimization for multiuser communications is proposed to optimize BS beamforming and RIS settings under hardware constraints. Further, the localization problem is addressed in the presence of faulty RIS elements. Based on the faulty RIS element detection algorithm, the signal quality variation of the high-dimensional data from RIS can be compensated thus enhance the positioning accuracy [41]. However, most of these studies have concentrated on the development of beamforming algorithms for RIS, neglecting to leverage the stability of the indoor propagation channel to propose a location-based signal enhancement scheme that reduces pilot overhead.

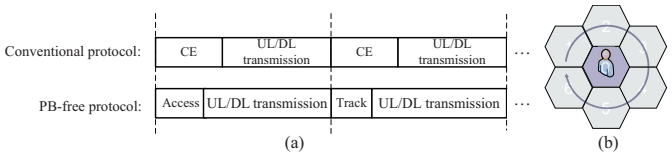

Fig. 1. Toy example of proposed PB-based transmission protocol: (a) Protocol comparison: A comparison between the conventional transmission protocol and the proposed PB-based protocol, where the access and track phase are used to retrieve the optimal RIS reflective pattern. (b) Tracking methodology: A simplified demonstration of RIS reflective pattern coverage after offline pre-design. User mobility is limited to adjacent cells, leading to 7 candidate reflective patterns, allowing real-time RIS optimization to be replaced by tracking retrieval.

In this paper, the objective is to present a transmission protocol for indoor RIS-aided communication systems that excludes CE, aiming to mitigate the need for extensive pilot overhead. The key idea is to design a location-based reflective pattern codebook, allowing the RIS to select reflective patterns from the codebook instead of relying on real-time optimization using estimated CSI, so called pre-designed beam (PB)-based protocol. A simplified illustration is provided in Fig. 1(a), where the transmission protocol is depicted, comprising two stages: the access stage and the tracking stage. During the access phase, occurring in the initial time slot, the AP identifies the optimal reflective pattern from a pre-designed codebook without CSI; In the tracking stage, as shown in Fig. 1(b), the AP conducts a search among the nearest reflective patterns (e.g., 7) and dynamically switches to the optimal one in response to UE movement, again without the use of CSI.

The main contributions can be summarized as follows:

1) We evaluate the channel gain provided by the RIS utilizing the EM-compliant RIS model, taking into account the near-field spherical waves. Subsequently, we derive a tight approximation of the channel gain degradation in the presence of location mismatch.
2) We design a location-based codebook that allows for efficient coverage with a minimal codebook size. Each codeword corresponds to a specific spatial sampling point, named representative point (RP), selected based on theoretical analysis. Through simulations, we demonstrate that our proposed location-based codebook surpasses the performance of the uniform topology of RPs and achieves superior coverage with a smaller codebook size.
3) We introduce a PB-based protocol. The proposed protocol eliminates the need for channel estimation by utilizing the location-based codebook. We also propose efficient retrieval strategies for both stages to minimize the pilot overhead required for selecting reflective patterns. Simulations demonstrate that our transmission protocol achieves higher achievable spectral efficiency (SE)

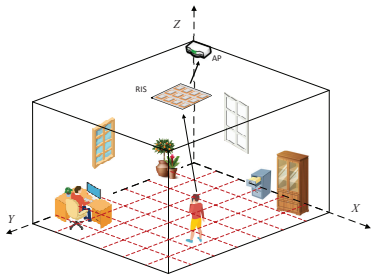

Fig. 2. An indoor RIS-assisted system with a RIS being hung from the ceiling.

compared to protocols that rely on channel estimation, particularly when considering the pilot overhead.

The remainder of the paper is structured as follows. Section II introduces the system model for the indoor RIS-aided system. Section III presents the results of the channel gain analysis and coverage limit analysis. In Section IV, a PB-based transmission protocol is proposed in the indoor RIS-aided system. Section V presents the numerical results, and Section VI summarizes the key findings. Proofs are provided in the appendices.

Throughout the paper, vectors and matrices are denoted in bold lowercase $\mathbf{a}$ and bold uppercase $\mathbf{A}$. The complex fields are represented by $\mathbb{C}$. The notation $\angle$ and $\|\cdot\|$ stand for the angle and the Frobenius norm of the input, respectively. The superscripts $(\cdot)^T$ and $(\cdot)^H$ denote transpose and conjugate-transpose operations.

II. System Model & Challenges

A. System Model

We consider an indoor scenario of $2L \times 2L$ where a single-antenna access point (AP) is positioned at the corner of the ceiling to ensure the AP-RIS channel link is unobstructed, and a single-antenna user is randomly deployed within the room. We assume an RIS is placed at the center of the room on the ceiling to enhance the coverage. The RIS is a uniform plane array (UPA) composed of $N \times N$ tunable elements driven by a controller to adjust the reflective coefficients. For ease of analysis, we define the coordinate of AP and UE as $\mathbf{o}_{\text{a}} \triangleq (x_a, y_a, z_a) = (L, L, z_h)$ and $\mathbf{o}_{\text{u}} \triangleq (x_u, y_u, z_u) = (x_u, y_u, 0)$, respectively, and the $(1,1)$th unit on RIS is located at $\mathbf{o}_{\text{r},1,1} \triangleq (x_{1,1}, y_{1,1}, z_{1,1}) = (0, 0, z_h)$. Then, assuming a unit spacing of $d = \lambda/2$ with λ being the wavelength, the coordinates of the (n, n')th unit can be expressed as $\mathbf{o}_{\text{r},n,n'} \triangleq (x_{n,n'}, y_{n,n'}, z_{n,n'}) = ((n-1)\lambda/2, (n'-1)\lambda/2, z_h)$.

We assume a line-of-sight (LoS) channel[1] in the near-field scenarios, where the AP-UE, AP-RIS and RIS-UE channel are modeled under the spherical wave assumption instead of the plane wave and are given as $h_{\text{d}} = e^{-j\kappa r_{\text{au}}}$, $\mathbf{g} = \mathbf{a}(r_{\text{ar}}, N, N)$ and $\mathbf{h}_{\mathbf{o}_{\text{u}}} = \mathbf{a}(r_{\text{ru}}, N, N)$, where $\mathbf{a}(r_{\text{ar(ru)}}, N, N) = \left[e^{-j\kappa r_{\text{ar(ru)},1,1}}, \ldots, e^{-j\kappa r_{\text{ar(ru)},N,N}}\right]^H \in \mathbb{C}^{N^2 \times 1}$ is the steering vector for the near-field channel with $\kappa = 2\pi/\lambda$, $r_{\text{au}} = \|\mathbf{o}_u - \mathbf{o}_a\|$ is the distance between the AP and UE, and $r_{\text{ar(ru)},n,n'}$ being the distance between the AP(UE) and the (n, n')th unit on RIS, which is given by

$$r_{\text{ru},n,n'} = \sqrt{(x_u - x_{n,n'})^2 + (y_u - y_{n,n'})^2 + z_h^2},$$
$$r_{\text{ar},n,n'} = \sqrt{(x_a - x_{n,n'})^2 + (y_a - y_{n,n'})^2}.$$

For ease of analysis, we measure the coordinates and the distance by the wavelength λ, i.e.,

$$\begin{aligned}&\left\{(x_u, y_u, z_u), (x_{n,n'}, y_{n,n'}, z_{n,n'}), (x_a, y_a, z_a)\right\} \\ &= \left\{(k_u, k_u, 0), \left(k_{x_{n,n'}}, k_{y_{n,n'}}, k_{z_h}\right), (k_L, k_L, k_{z_h})\right\}\lambda, \quad (1)\end{aligned}$$

where $k_{x_{n,n'}} = \frac{n-1}{2}$ and $k_{y_{n,n'}} = \frac{n'-1}{2}$ and the steering vector can be represented as

$$\mathbf{a}(k_{r_{\text{ar(ru)}}}, N, N) = \left[e^{-j2\pi k_{r_{\text{ar(ru)},1,1}}}, \ldots, e^{-j2\pi k_{r_{\text{ar(ru)},N,N'}}}\right]^H$$

with

$$k_{r_{\text{ru},n,n'}} = \sqrt{\left(k_{x_u} - \tfrac{n-1}{2}\right)^2 + \left(k_{y_u} - \tfrac{n'-1}{2}\right)^2 + k_{z_h}^2}, \quad (2)$$

$$k_{r_{\text{ar},n,n'}} = \sqrt{\left(k_L - \tfrac{n-1}{2}\right)^2 + \left(k_L - \tfrac{n'-1}{2}\right)^2}. \quad (3)$$

Applying an electromagnetic-compliant complex channel model to describe the signal, we can express the received signal as [43]

$$r_{\mathbf{o}_{\text{u}}}(\mathbf{\Phi}) = \left(h_{\text{d}} + \mathbf{g}^T \mathbf{\Phi} \mathbf{h}_{\mathbf{o}_{\text{u}}}\right) s + w, \quad (4)$$

where $s \sim \mathcal{CN}(0,1)$ and $w \sim \mathcal{CN}(0, \sigma^2)$ are the transmitted signal and the noise, respectively. $\mathbf{\Phi} = (\mathbf{Z}_{\text{ss}} + \mathbf{Z}_{\text{ris}})^{-1}$ can be viewed as reflection coefficients [43] with $\mathbf{Z}_{\text{ss}}$ being the $N^2 \times N^2$ mutual impedances matrix between reconfigurable elements of the RIS. $\mathbf{Z}_{\text{ris}}$ is the diagonal matrix representing the tunable impedances. The real part of the ith diagonal entry $\Re\{z_{\text{ris},i}\} = r_0 \geq 0$ denotes the fixed resistance that accounts for the internal losses, and the imaginary part $\Im\{z_{\text{ris},i}\}$ represents the reactance and can be set to an arbitrary value for system optimization.

B. Challenges

The aim of the paper is to propose a transmission protocol to address the excessive pilot consumption problem in RIS-assisted communication systems, as shown in Fig. 1. The main idea is to involve the pre-design of a codebook consisting of reflective patterns for the RIS, which enables the RIS to dynamically switch between patterns and select the one that offers the highest quality of service without requiring CSI, turning the CE problem into a searching problem. However, the idea brings two important issues:

- *Principles of codebook design*. To enhance the precision of the beam reflected by the RIS, it is generally recommended to design a codebook with a large size that covers all possible locations in the room. A sufficiently large codebook makes it feasible to identify an appropriate reflective pattern that can accurately beam toward a UE

[1] In indoor propagation environments, both line-of-sight (LoS) and non-line-of-sight (NLoS) paths contribute to Rician channels. According to empirical measurements in [42], the signal strength from the LoS path notably surpasses that of the NLoS path in the bands above the mmWave. Therefore, we simplify the channel model accordingly to provide more insights. As depicted in Fig. 6, the performance of a Rician channel remains largely unaffected when NLoS CSI is not available.

at any location. However, a codebook that is excessively large can introduce significant delays in the process of retrieving the appropriate pattern, leading to latency issues. Therefore, there is an urgent need to propose a suitable spatial sampling principle to determine RPs to reduce the codebook size while ensuring coverage.

- *Codebook indexing algorithm*. The movement of UE can lead to a mismatch between the reflective pattern and the UE's actual location. This necessitates the RIS to adjust its configuration multiple times during transmission to maintain signal quality. However, it is impractical to retrieve the entire codebook for each change, as it would compromise communication stability. Therefore, it is crucial to develop an efficient indexing algorithm that enables quick and accurate retrieval of the most suitable reflective pattern for the UE's location.

III. Channel Gain Analysis

In this section, our objective is to examine the channel gain provided by the RIS in indoor scenarios and establish a theoretical foundation for the design of reflective pattern codebooks.

A. Ideal Channel Gain

In the presence of perfect CSI, the optimal configuration of the RIS ensures that the phases of the reflected signals from each reflective unit are adjusted to align at the receiver.

If we denote by $z_{\mathbf{o}_\mathrm{u}}(\mathbf{\Phi}) = h_\mathrm{d} + \mathbf{g}^T\mathbf{\Phi}\mathbf{h}_{\mathbf{o}_\mathrm{u}}$ the cascaded channel, we simplify the signal as

$$r_{\mathbf{o}_\mathrm{u}}(\mathbf{\Phi}) = z_{\mathbf{o}_\mathrm{u}}(\mathbf{\Phi})\, s + w, \tag{5}$$

and the corresponding channel gain at $\mathbf{o}_\mathrm{u}$ can be computed as

$$\mathcal{G}_{\mathbf{o}_\mathrm{u}} = \left|z_{\mathbf{o}_\mathrm{u}}(\mathbf{\Phi})\right|^2. \tag{6}$$

Utilizing a similar methodology as presented in [43] and assuming no mutual coupling, the channel can be rewritten as follows:

$$z_{\mathbf{o}_\mathrm{u}}(\mathbf{\Phi}) = h_\mathrm{d} + \sum_{n=1}^{N}\sum_{n'=1}^{N}\frac{g_{n,n'}h_{n,n'}}{z_{\mathrm{ss},n,n'}+z_{\mathrm{ris},n,n'}}, \tag{7}$$

where $g_{n,n'}$ and $h_{n,n'}$ are the (n,n')-th element in $\mathbf{g}$ and $\mathbf{h}_{\mathbf{o}_\mathrm{u}}$, and $z_{\mathrm{ss},n,n'}$ and $z_{\mathrm{ris},n,n'}$ is the $\big((n-1)N+n'\big)$-th diagonal element in $\mathbf{Z}_\mathrm{ss}$ and $\mathbf{Z}_\mathrm{ris}$, respectively. Moreover, denote by $r_{n,n'} = \Re\{z_{\mathrm{ris},n,n'} + z_{\mathrm{ss},n,n'}\}$, we can obtain [43]

$$\frac{1}{z_{\mathrm{ss},n,n'} + z_{\mathrm{ris},n,n'}} = \frac{1+e^{j\theta_{\mathbf{o}_\mathrm{u},n,n'}}}{2\left|r_{n,n'}\right|}, \tag{8}$$

where $\theta_{\mathbf{o}_\mathrm{u},n,n'} \in [-\pi,\pi)$ is the tunable phase controlled by the (n,n')th reflective unit. Recall the definitions of $\Re\{z_{\mathrm{ris},n,n'}\}$ and $\Re\{z_{\mathrm{ss},n,n'}\}$, $r_{n,n'}$ are identical across $N\times N$ elements, i.e., $r_0 = r_{n,n'}, \forall n,n'$. Therefore, we have the equivalent channel $z_{\mathbf{o}_\mathrm{u}}(\mathbf{\Phi}) = z_{\mathbf{o}_\mathrm{u}}(\boldsymbol{\theta})$ with

$$z_{\mathbf{o}_\mathrm{u}}(\boldsymbol{\theta}) = \underbrace{\tau}_{\text{non-tunable}} + \underbrace{\tfrac{1}{2r_0}\sum_{n=1}^{N}\sum_{n'=1}^{N}a_{n,n'}e^{j\theta_{\mathbf{o}_\mathrm{u},n,n'}}}_{\text{tunable}}, \tag{9}$$

where $a_{n,n'} = g_{n,n'}h_{n,n'}$ and $\tau = h_\mathrm{d} + \frac{b}{2r_0}$ with $b = \sum_{n=1}^{N}\sum_{n'=1}^{N}a_{n,n'}$.

Denote by $\varphi_\tau = \angle\tau$ and $\varphi_{a_{n,n'}} = \angle a_{n,n'}$ the angle of the corresponding coefficients. In order to maximize the channel gain, the optimal reflective coefficient of the (n,n')-th element can be determined by aligning the phases of the signals from each reflective path, given by

$$\theta^*_{\mathbf{o}_\mathrm{u},n,n'} = -\angle\left(\tau a^H_{n,n'}\right) = \varphi_{a_{n,n'}} - \varphi_\tau, \tag{10}$$

in such a way that all components have the same phase φ_b. Letting $c^*_{n,n'} = a_{n,n'}e^{j\theta^*_{\mathbf{o}_\mathrm{u},n,n'}}$, the reconfigured channel can be expressed as $z_{\mathbf{o}_\mathrm{u}}(\boldsymbol{\theta}^*_{\mathbf{o}_\mathrm{u}}) = \tau + \frac{1}{2r_0}\sum_{n=1}^{N}\sum_{n'=1}^{N}c^*_{n,n'}$, and the corresponding channel gain achieves its optimal value

$$\begin{aligned}\mathcal{G}_{\mathbf{o}_\mathrm{u}} &= \left|z_{\mathbf{o}_\mathrm{u}}\left(\boldsymbol{\theta}^*_{\mathbf{o}_\mathrm{u}}\right)\right|^2 \\ &= \left|\tau + \tfrac{1}{2r_0}\sum\nolimits_{n=1}^{N}\sum\nolimits_{n'=1}^{N}c^*_{n,n'}\right|^2.\end{aligned} \tag{11}$$

Proposition 1: With the optimal reflective profile $\boldsymbol{\theta}^*_{\mathbf{o}_\mathrm{u}}$ at the RIS, the overall reflective channel for a UE located at $\mathbf{o}_\mathrm{u}$ can be approximated by (12) at the top of the next page, and the corresponding channel gain is given by (13), where $f(a) = \frac{\sin(Na/2)}{\sin(a/2)}$, $A^* = 2\pi\left(k_{r_\mathrm{ru}} + \frac{k_{x_u}+k_{y_u}}{2k_{r_\mathrm{ru}}} + \sqrt{2}k_L + \frac{1}{\sqrt{2}}\right)$, $B^* = -2\pi\left(\frac{k_{x_u}}{2k_{r_\mathrm{ru}}} + \frac{1}{2\sqrt{2}}\right)$, and $C^* = -2\pi\left(\frac{k_{y_u}}{2k_{r_\mathrm{ru}}} + \frac{1}{2\sqrt{2}}\right)$ with k_{r_ru} representing the distance between $\mathbf{o}_\mathrm{u}$ and $\mathbf{o}_{\mathrm{r},1,1}$.[2]

Proof: See Appendix A. ∎

The expressions for the overall channel and the corresponding channel gain are notably complex, with both magnitude and phase varying depending on the user's precise location, making it challenging to extract valuable insights from theoretical results. However, given the typically extensive array of reflective units in RIS, it is reasonable to assume that the gain provided by the reflective channel from the RIS far exceeds the channel gain attributable to the AP-UE path. Therefore, in the later section, we present the channel gain analysis without considering the AP-UE path, and the received signal as well as the corresponding equivalent channel are given by:

$$\tilde{r}_{\mathbf{o}_\mathrm{u}}(\mathbf{\Phi}) = \mathbf{g}^T\mathbf{\Phi}\mathbf{h}_{\mathbf{o}_\mathrm{u}}s + w, \tag{14}$$

and

$$\tilde{z}_{\mathbf{o}_\mathrm{u}}(\boldsymbol{\theta}) = b + \tfrac{1}{2r_0}\sum_{n=1}^{N}\sum_{n'=1}^{N}a_{n,n'}e^{j\theta_{\mathbf{o}_\mathrm{u},n,n'}}. \tag{15}$$

Corollary 1: Assuming obstructed AP-UE link, with the optimal reflective profile $\boldsymbol{\theta}^*_{\mathbf{o}_\mathrm{u}}$ at the RIS, the overall reflective channel for a UE located at $\mathbf{o}_\mathrm{u}$ can be approximated by

$$\tilde{z}_{\mathbf{o}_\mathrm{u}}(\boldsymbol{\theta}^*_{\mathbf{o}_\mathrm{u}}) = \tfrac{1}{2r_0}\left(N^2 + f(B^*)f(C^*)\right)e^{-j\left(A^* + \frac{N+1}{2}(B^*+C^*)\right)}, \tag{16}$$

and the corresponding channel gain is given by

$$\tilde{\mathcal{G}}_{\mathbf{o}_\mathrm{u}}(\boldsymbol{\theta}^*_{\mathbf{o}_\mathrm{u}}) = \tfrac{1}{4r_0^2}\left(N^2 + \left|f(B^*)\right|\left|f(C^*)\right|\right)^2, \tag{17}$$

where $A^* = 2\pi\left(k_{r_\mathrm{ru}} + \frac{k_{x_u}+k_{y_u}}{2k_{r_\mathrm{ru}}} + \sqrt{2}k_L + \frac{1}{\sqrt{2}}\right)$, $B^* = -2\pi\left(\frac{k_{x_u}}{2k_{r_\mathrm{ru}}} + \frac{1}{2\sqrt{2}}\right)$, and $C^* = -2\pi\left(\frac{k_{y_u}}{2k_{r_\mathrm{ru}}} + \frac{1}{2\sqrt{2}}\right)$ with k_{r_ru} representing the distance between $\mathbf{o}_\mathrm{u}$ and $\mathbf{o}_{\mathrm{r},1,1}$.

[2]For the sake of brevity, we use the notation k_{r_ru} to refer specifically to $k_{r_\mathrm{ru},1,1}$ throughout this paper.

$$z_{\mathbf{o}_\mathrm{u}}(\boldsymbol{\theta}^*_{\mathbf{o}_\mathrm{u}}) = \left(\frac{N^2}{2r_0} + \sqrt{\left(1 + \frac{f(B^*)^2 f(C^*)^2}{4r_0^2} + \frac{f(B^*)f(C^*)}{r_0}\cos\left(A^* + \frac{N+1}{2}\left(B^*+C^*\right) - \kappa r_{\mathrm{au}}\right)\right)}\right) \times e^{-j\left(\arctan\frac{\sin(\kappa r_{\mathrm{au}}) + \frac{1}{2r_0} f(B^*)f(C^*)\sin\left(A^* + \frac{N+1}{2}(B^*+C^*)\right)}{\cos(\kappa r_{\mathrm{au}}) + \frac{1}{2r_0} f(B^*)f(C^*)\cos\left(A^* + \frac{N+1}{2}(B^*+C^*)\right)}\right)} \tag{12}$$

$$\mathcal{G}_{\mathbf{o}_\mathrm{u}}(\boldsymbol{\theta}^*_{\mathbf{o}_\mathrm{u}}) = \left(\frac{N^2}{2r_0} + \sqrt{\left(1 + \frac{f(B^*)^2 f(C^*)^2}{4r_0^2} + \frac{f(B^*)f(C^*)}{r_0}\cos\left(A^* + \frac{N+1}{2}\left(B^*+C^*\right) - \kappa r_{\mathrm{au}}\right)\right)}\right)^2 \tag{13}$$

Proof: The result can be obtained using the same method as Appendix A by setting $h_\mathrm{d} = 0$. ∎

Remark 1: From *Corollary 1*, the impact of the non-tunable parts, i.e., $|f(B^*)|$ and $|f(C^*)|$, on the channel gain exhibits a decreasing trend with oscillations as the number of units, N^2, increases. This observation suggests that the controllable part of the RIS becomes more influential in determining the channel gain with more units. This behavior is particularly significant considering that practical RIS implementations often involve a large number of reflective units. As a result, the contribution from the non-tunable part becomes almost negligible. In this case, the reflective model of RIS can be simplified from $\frac{1+e^{j\theta_i}}{2r_0}$ to $\frac{e^{j\theta_i}}{2r_0}$, and the channel gain expression is reduced to $\tilde{\mathcal{G}}_{\mathbf{o}_\mathrm{u}}(\boldsymbol{\theta}^*_{\mathbf{o}_\mathrm{u}}) = \frac{N^4}{4r_0^2}$. This simplified model aligns with the classic model and further demonstrates the generality of the electromagnetic-compliant model presented in (8).

B. Channel Gain with Location Mismatch

In practical scenarios, the location of the UE may vary over time, resulting in variations in the channel. As a result, the reflective pattern optimized for a specific location $\mathbf{o}_\mathrm{u}$ may not remain optimal when the UE moves. It is worth noting that minor movements of the UE may not have a significant impact on the channel, and it is only when the UE moves a significant distance causing substantial changes in the channel that switching the reflective pattern becomes necessary. Therefore, to design an efficient location-based reflective pattern codebook, evaluating the performance degradation from location mismatch is crucial. This assists in optimizing the tradeoff between codebook size and signal quality by setting an appropriate performance loss threshold.

Assume that the UE moves on the xy plane from $\mathbf{o}_\mathrm{u}$ to $\tilde{\mathbf{o}}_\mathrm{u} \triangleq (\tilde{x}_u, \tilde{y}_u, 0)$, the (n,n')-th entry of the RIS-UE channel at $\tilde{\mathbf{o}}_\mathrm{u}$ is given by $\tilde{h}_{n,n'} = e^{-j2\pi k_{\tilde{r}_{\mathrm{ru}},n,n'}}$ with $k_{\tilde{r}_{\mathrm{ru}},n,n'} = \sqrt{\left(k_{\tilde{x}_u} - \frac{n-1}{2}\right)^2 + \left(k_{\tilde{y}_u} - \frac{n'-1}{2}\right)^2 + k_{z_h}^2}$ representing the distance in number of waves. Given the optimal reflective pattern at $\mathbf{o}_\mathrm{u}$, the received signal for UE at $\tilde{\mathbf{o}}_\mathrm{u}$ is represented as

$$\tilde{r}_{\tilde{\mathbf{o}}_\mathrm{u}}\left(\boldsymbol{\theta}^*_{\mathbf{o}_\mathrm{u}}\right) = \underbrace{\frac{1}{2r_0}\left(\sum_{n=1}^{N}\sum_{n'=1}^{N}\tilde{a}_{n,n'} + \tilde{a}_{n,n'}e^{j\theta^*_{\mathbf{o}_\mathrm{u},n,n'}}\right)}_{z_{\tilde{\mathbf{o}}_\mathrm{u}}\left(\boldsymbol{\theta}^*_{\mathbf{o}_\mathrm{u}}\right)} s + w, \tag{18}$$

where $\tilde{a}_{n,n'} = g_{n,n'}\tilde{h}_{n,n'}$, and the corresponding channel gain is given by

$$\tilde{\mathcal{G}}_{\tilde{\mathbf{o}}_\mathrm{u}} = \left|z_{\tilde{\mathbf{o}}_\mathrm{u}}(\boldsymbol{\theta}^*_{\mathbf{o}_\mathrm{u}})\right|^2. \tag{19}$$

Next, we proceed to evaluate the degradation in channel gain resulting from the location mismatch. As illustrated in Fig. 3, where the UE's movement is characterized by the distance v and the direction ω, the coordinates of the new position can be expressed as $\tilde{\mathbf{o}}_\mathrm{u} = (k_{x_u} + k_{\hat{x}_u}, k_{y_u} + k_{\hat{y}_u}, 0)\lambda$ where $k_{\hat{x}_u} = k_v \sin\omega$ and $k_{\hat{y}_u} = k_v \cos\omega$ with $k_v = v/\lambda$.

Proposition 2: With the optimal reflective pattern for position $\mathbf{o}_\mathrm{u}$, the overall channel at the location $\tilde{\mathbf{o}}_\mathrm{u}$ can be approximated by

$$\tilde{z}_{\tilde{\mathbf{o}}_\mathrm{u}}(\boldsymbol{\theta}^*_{\mathbf{o}_\mathrm{u}}) = \frac{1}{2r_0}\left(\frac{\sin\left(N\bar{B}/2\right)\sin\left(N\bar{C}/2\right)}{\sin\left(\bar{B}/2\right)\sin\left(\bar{C}/2\right)}e^{-j\left(\bar{A}+\frac{N+1}{2}\left(\bar{B}+\bar{C}\right)\right)} + \frac{\sin\left(N\tilde{B}/2\right)\sin\left(N\tilde{C}/2\right)}{\sin\left(\tilde{B}/2\right)\sin\left(\tilde{C}/2\right)}e^{-j\left(\tilde{A}+\frac{N+1}{2}\left(\tilde{B}+\tilde{C}\right)\right)}\right), \tag{20}$$

where $\bar{A}$ and $\tilde{A}$ are given at the top of the next page, and

$$\bar{B} = 2\pi\left(\frac{k_{\hat{x}_u} - k_{x_u}}{2f(k_{r_{\mathrm{ru}}},k_v,k_u(\omega))} - \frac{\sqrt{2}}{4}\right), \tag{21a}$$

$$\tilde{B} = 2\pi\left(\frac{k_{\hat{x}_u} - k_{x_u}}{2f(k_{r_{\mathrm{ru}}},k_v,k_u(\omega))} + \frac{k_{x_u}}{2k_{r_{\mathrm{ru}}}}\right), \tag{21b}$$

$$\bar{C} = 2\pi\left(\frac{k_{\hat{y}_u} - k_{y_u}}{2f(k_{r_{\mathrm{ru}}},k_v,k_u(\omega))} - \frac{\sqrt{2}}{4}\right), \tag{21c}$$

$$\tilde{C} = 2\pi\left(\frac{k_{\hat{y}_u} - k_{y_u}}{2f(k_{r_{\mathrm{ru}}},k_v,k_u(\omega))} + \frac{k_{y_u}}{2k_{r_{\mathrm{ru}}}}\right), \tag{21d}$$

with $f(k_{r_{\mathrm{ru}}}, k_v, k_u(\omega)) = \sqrt{k_{r_{\mathrm{ru}}}^2 + k_v^2 - 2k_v k_u(\omega)}$ and $k_u(\omega) = \sqrt{k_{x_u}^2 + k_{y_u}^2}\sin(\omega + \tan^{-1}\frac{k_{y_u}}{k_{x_u}})$.

Proof: See Appendix B. ∎

Proposition 2 demonstrates that the non-tunable and controllable parts of the channel have different phases, making it challenging to determine the overall phase and channel gain. However, when the number of units N^2 is fixed, the amplitudes of both parts are expected to decrease in an oscillating manner as $\hat{B}$, $\tilde{B}$, $\hat{C}$, and $\tilde{C}$ increase. Moreover, as discussed in *Remark* 1, the contribution from the non-tunable components becomes negligible when N is large. Therefore, we can ignore the non-tunable part and obtain an approximate channel gain with location mismatch, which allows us to gain valuable insights.

Proposition 3: With the optimal reflective pattern for position $\mathbf{o}_\mathrm{u}$, the channel gain at the location $\tilde{\mathbf{o}}_\mathrm{u}$ can be approximated by

$$\tilde{\mathcal{G}}_{\tilde{\mathbf{o}}_\mathrm{u}}(\boldsymbol{\theta}^*_{\mathbf{o}_\mathrm{u}}) = \frac{1}{4r_0^2}\left|\frac{\sin\left(N\tilde{B}/2\right)}{\sin(\tilde{B}/2)}\right|^2\left|\frac{\sin\left(N\tilde{C}/2\right)}{\sin(\tilde{C}/2)}\right|^2. \tag{23}$$

$$\bar{A} = 2\pi \left(f\left(k_{r_{\rm ru}}, k_v, k_u(\omega)\right) + \frac{k_{x_u}+k_{y_u}-k_{\hat{x}_u}-k_{\hat{y}_u}}{2f(k_{r_{\rm ru}},k_v,k_u(\omega))} + \sqrt{2}k_L + \frac{\sqrt{2}}{2} \right)$$
$$\tilde{A} = 2\pi \left(f\left(k_{r_{\rm ru}}, k_v, k_u(\omega)\right) + \frac{k_{x_u}+k_{y_u}-k_{\hat{x}_u}-k_{\hat{y}_u}}{2f(k_{r_{\rm ru}},k_v,k_u(\omega))} - k_{r_{\rm ru}} - \frac{k_{x_u}+k_{y_u}}{2k_{r_{\rm ru}}} \right) + \varphi_b$$

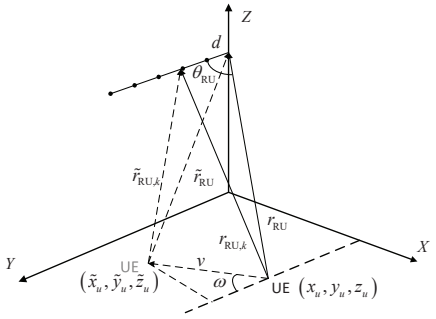

Fig. 3. A diagram of the variation of UE position.

Proof: The result can be obtained by removing the non-tunable part from (20), and squaring the absolute value of amplitude of the remaining terms. ■

Proposition 3 shows the sensitivity of the channel gain to the location offset and reveals the relationship between the location offset, the UE position $\mathbf{o}_{\rm u}$ and the channel gain. However, it is not easy to draw meaningful insights directly due to the complex relationships between variables $\tilde{B}$ and $\tilde{C}$ and the location offset. Therefore, we conduct further investigations into the relationship between coverage and channel gain in the subsequent subsections.

C. Coverage limit

In this subsection, our objective is to address the following problem: Given a minimum ratio $\gamma \subset (0,1)$, we aim to determine the range centered on $\mathbf{o}_{\rm u}$ for which the channel gain is not lower than $\gamma\tilde{\mathcal{G}}_{\mathbf{o}_{\rm u}}(\boldsymbol{\theta}^*_{\mathbf{o}_{\rm u}})$ with $\boldsymbol{\theta}^*_{\mathbf{o}_{\rm u}}$ being the reflective pattern.

Utilizing *Proposition* 3, we observe that the maximum channel gain at $\mathbf{o}_{\rm u}$ occurs when $k_v \to 0$. Hence, (23) can be simplified as

$$\tilde{\mathcal{G}}_{\tilde{\mathbf{o}}_{\rm u}}\left(\boldsymbol{\theta}^*_{\mathbf{o}_{\rm u}}\right) \xrightarrow{k_v \to 0} \frac{N^4}{4r_0^2}.$$

The result can be obtained by having $\tilde{B}, \tilde{C} \xrightarrow{k_v \to 0} 0$, and using limits $\frac{\sin(Nx)}{\sin(x)} \xrightarrow{k_v \to 0} N$. Therefore, the target problem can be formulated as

$$\mathcal{P}1: \ \arg\min_{k_v} \ \tilde{\mathcal{G}}_{\tilde{\mathbf{o}}_{\rm u}}\left(\boldsymbol{\theta}^*_{\mathbf{o}_{\rm u}}\right) \tag{24a}$$
$$\text{s.t.} \ \ \tilde{\mathcal{G}}_{\tilde{\mathbf{o}}_{\rm u}}\left(\boldsymbol{\theta}^*_{\mathbf{o}_{\rm u}}\right) \geq \frac{\gamma N^4}{4r_0^2}. \tag{24b}$$

Since $\tilde{\mathcal{G}}_{\tilde{\mathbf{o}}_{\rm u}}\left(\boldsymbol{\theta}^*_{\mathbf{o}_{\rm u}}\right)$ is a monotonically decreasing function in the area near of $k_v = 0$, we can find the solution for k_v by solving the equation $\tilde{\mathcal{G}}_{\tilde{\mathbf{o}}_{\rm u}}\left(\boldsymbol{\theta}^*_{\mathbf{o}_{\rm u}}\right) = \frac{\gamma N^4}{4r_0^2}$. The root of this equation represents the range centered at $\mathbf{o}_{\rm u}$ where the channel gain is not lower than $\gamma\tilde{\mathcal{G}}_{\mathbf{o}_{\rm u}}(\boldsymbol{\theta}^*_{\mathbf{o}_{\rm u}})$. To simplify the evaluation, we introduce two additional variables, $\gamma_B \subset (0,1)$ and $\gamma_C \subset (0,1)$, as thresholds to measure the channel gain loss along the x-axis and y-axis, respectively. In this way, the problem $\mathcal{P}1$ can be decomposed into the following set of equations:

$$\mathcal{P}2: \ \begin{cases} \frac{\sin\left(N\tilde{B}/2\right)}{\sin(\tilde{B}/2)} = N\gamma_B \\ \frac{\sin\left(N\tilde{C}/2\right)}{\sin(\tilde{C}/2)} = N\gamma_c \\ \gamma_B\gamma_c = \gamma \end{cases}. \tag{25}$$

Proposition 4: Given a reflective pattern $\boldsymbol{\theta}^*_{\mathbf{o}_{\rm u}}$, to ensure the channel gain is not less than $\frac{\gamma N^2}{4r_0^2}$, the coverage area defined by the range of k_v should satisfy the following condition:

$$k_v(k_{r_{\rm ru}}, \omega) = k_u(\omega) + \sqrt{k_{r_{\rm ru}}^2 + k_u^2(\omega) - \frac{k_{z_h}^2}{1-4J_{\mathbf{o}_{\rm u}}(N,\gamma_B,\gamma_C)}} \tag{26}$$

with $\gamma = \gamma_B\gamma_C$, where $J_{\mathbf{o}_{\rm u}}(N,\gamma_B,\gamma_C) = \left(\frac{\text{sinc}^{-1}\gamma_B}{N\pi} - \frac{k_{x_u}}{2k_{r_{\rm ru}}}\right)^2 + \left(\frac{\text{sinc}^{-1}\gamma_C}{N\pi} - \frac{k_{y_u}}{2k_{r_{\rm ru}}}\right)^2$ with $\text{sinc}^{-1}(a)$ being the first positive solution of $a = \text{sinc}(x)$.

Proof: See Appendix C. ■

The obtained result reveals that the attenuation of the channel gain is dependent on the direction ω. Specifically, the channel gain exhibits the slowest decrease along the direction from the RIS to $\mathbf{o}_{\rm u}$, and the fastest decrease in the opposite direction. This phenomenon can be observed through the following corollary.

Corollary 2: Given a reflective pattern $\boldsymbol{\theta}^*_{\mathbf{o}_{\rm u}}$, to ensure the channel gain is not less than $\frac{\gamma N^2}{4r_0^2}$, the coverage range defined by $k_v(k_{r_{\rm ru}}, \omega)$ reaches the maximum and the minimum at the directions $\omega_{\max} = \tan^{-1}\frac{k_{x_u}}{k_{y_u}}$ and $\omega_{\min} = \pi + \tan^{-1}\frac{k_{x_u}}{k_{y_u}}$, and are given by

$$k_v\left(k_{r_{\rm ru}}, \omega_{\max}\right) = E(k_{r_{\rm ru}}) + \sqrt{k_{r_{\rm ru}}^2 - k_{z_h}^2}, \tag{27}$$
$$k_v\left(k_{r_{\rm ru}}, \omega_{\min}\right) = E(k_{r_{\rm ru}}) - \sqrt{k_{r_{\rm ru}}^2 - k_{z_h}^2} \tag{28}$$

with $E(k_{r_{\rm ru}}) = \sqrt{2k_{r_{\rm ru}}^2 - k_{z_h}^2 - \frac{k_{z_h}^2}{1-4J_{\mathbf{o}_{\rm u}}(N,\gamma_B,\gamma_C)}}$.

Proof: Taking the first derivative of $k_v(k_{r_{\rm ru}}, \omega)$ w.r.t ω and setting $\partial k_v(k_{r_{\rm ru}}, \omega)/\partial\omega = 0$, we yield $\omega^* = n\pi + \tan^{-1}\frac{k_{x_u}}{k_{y_u}}$. Observing that $k_v'(k_{r_{\rm ru}}, \omega_-^*) > 0$ and $k_v'(k_{r_{\rm ru}}, \omega_+^*) < 0$ at $\tan^{-1}\frac{k_{x_u}}{k_{y_u}}$, and opposite is true at $\pi + \tan^{-1}\frac{k_{x_u}}{k_{y_u}}$, we conclude that $\omega_{\min}$ and $\omega_{\max}$ correspond to the minimum and the maximum point of $k_v(\omega)$. Further, noting that $k_u(\omega_{\max}) = \sqrt{k_{x_u}^2 + k_{y_u}^2}$ and $k_u(\omega_{\min}) = -\sqrt{k_{x_u}^2 + k_{y_u}^2}$, after some manipulations, we complete the proof. ■

Remark 2: Given a fixed $k_{r_{\rm ru}}$, the coverage can be approximately sketched as an "elliptic-like" graph, with the major axis and minor axis roughly expressed as $k_v(k_{r_{\rm ru}}, \omega_{\min}) + k_v(k_{r_{\rm ru}}, \omega_{\max})$ and $k_v(k_{r_{\rm ru}}, \omega_{\min} + \frac{\pi}{2}) + k_v(k_{r_{\rm ru}}, \omega_{\max} + \frac{\pi}{2})$,

and are given by

$$k_v(k_{r_{\rm ru}},\omega_{\min})+k_v(k_{r_{\rm ru}},\omega_{\max})=2E(k_{r_{\rm ru}}), \tag{29}$$

$$k_v(k_{r_{\rm ru}},\omega_{\min}+\tfrac{\pi}{2})+k_v(k_{r_{\rm ru}},\omega_{\max}+\tfrac{\pi}{2}) = 2\sqrt{k_{r_{\rm ru}}^2-\frac{k_{z_h}^2}{1-4J_{\mathbf{o}_{\rm u}}(N,\gamma_B,\gamma_C)}}, \tag{30}$$

respectively. The minor axis can be obtained by $k_u(\omega_{\min}+\frac{\pi}{2})=k_u(\omega_{\max}+\frac{\pi}{2})=0$.

In order to give more insights, we further investigate the following two extreme scenarios:

- For the central area of the room, i.e., $\mathbf{o}_{\rm u}=(0,0,0)$, $k_v(k_{r_{\rm ru}},\omega)$ equals
$$k_v=\frac{2\beta k_{z_h}}{N\pi}\sqrt{\mathrm{sinc}^{-2}\gamma_{\tilde{B}}+\mathrm{sinc}^{-2}\gamma_{\tilde{C}}}, \tag{31}$$
where $\beta=\left(1-\frac{4}{N^2\pi^2}\left(\mathrm{sinc}^{-2}\gamma_{\tilde{B}}+\mathrm{sinc}^{-2}\gamma_{\tilde{C}}\right)\right)^{-\frac{1}{2}}$. The result can be obtained by substituting $k_{x_u}=k_{y_u}=0$ into (26).
- For the area at the edge of the room where $k_{r_{\rm ru}}\gg k_v$, $k_v(k_{r_{\rm ru}},\omega)$ approximates to
$$k_v=\frac{2k_{r_{\rm ru}}}{N\pi}\sqrt{\mathrm{sinc}^{-2}\gamma_{\tilde{B}}+\mathrm{sinc}^{-2}\gamma_{\tilde{C}}}, \tag{32}$$
and if $\mathbf{o}_{\rm u}$ is located at the corner, i.e., $k_{r_{\rm ru}}=\sqrt{2k_L^2+k_{z_h}^2}$, we have
$$k_v=\frac{2\sqrt{2k_L^2+k_{z_h}^2}}{N\pi}\sqrt{\mathrm{sinc}^{-2}\gamma_{\tilde{B}}+\mathrm{sinc}^{-2}\gamma_{\tilde{C}}} \tag{33}$$
by approximating $f\left(k_{r_{\rm ru}},k_v,\omega\right)\approx k_{r_{\rm ru}}$.

The results of the two extreme cases indicate that the coverage area of a reflective pattern is determined by the specific target location. In addition, since thresholds $\gamma_{\tilde{B}},\gamma_{\tilde{C}}\subset(0,1]$, we have $\mathrm{sinc}^{-1}\gamma_{\tilde{B}}\subset(0,\pi]$ and $\mathrm{sinc}^{-1}\gamma_{\tilde{C}}\subset(0,\pi]$. Due to the massive number of elements on RIS, the parameter β in (31) is typically slightly less than 1. When comparing equation (31) with (33), the coverage limits of the RIS reflective pattern are significantly larger in the corner region compared to the center region, as shown in Fig. 4. As a result, equations (31) and (33) can be considered as the lower bound and upper bound, respectively, for the coverage limits of a RIS reflective pattern. These results form a fundamental basis for the design of RIS reflective pattern codebooks in the following sections.

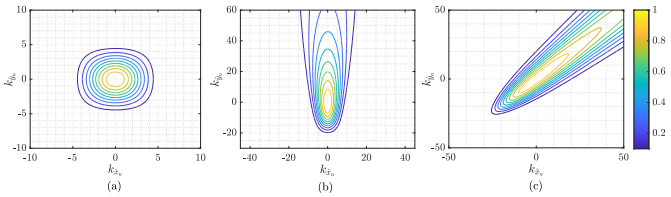

Fig. 4. The contour lines of the channel gain for a given reflective pattern targeted to different $\mathbf{o}_{\rm u}$, where (a) represents $\mathbf{o}_{\rm u}=(0,0,0)$, (b) represents $\mathbf{o}_{\rm u}=(50\lambda,0,0)$, and (c) represents $\mathbf{o}_{\rm u}=(100\lambda,100\lambda,0)$.

IV. PB-BASED TRANSMISSION PROTOCOL

Leveraging the established theoretical results, we can now tackle the challenges associated with codebook design, as discussed in Section II. B.

A. Location-based codebook design

To optimize the design of a codebook, it is crucial to ensure that the codewords are sufficiently "representative" to achieve a reduction in codebook size while still providing comprehensive coverage. In the context of indoor communication scenarios, the relatively stable propagation environment offers an opportunity for efficient location-based codebook design. By leveraging the channel gain analysis presented in *Proposition* 3, it is possible to identify the spatial samplings that can provide sufficiently "representative" for codebook design.

The topology of the RP is critical for the location-based codebook design. The ideal RPs should be the optimal spatial sampling points that have a distribution with an appropriate density to ensure that the coverage areas of the corresponding RIS reflective patterns are interconnected, and the channel gain at the junction of adjacent coverage areas remains above a predetermined threshold. Such a topology enables the RIS to track and switch the reflective pattern as the user moves from one coverage area to another while ensuring signal quality.[3]

1) Uniform topology: The uniform topology may not be the ideal choice for the spatial sampling principle of RPs due to the significant difference in coverage area between the center and edge regions of the room. As a result, the uniform RP topology can lead to non-uniform coverage across the room. However, the uniform topology offers a simple and straightforward solution, as the coordinates of the RPs can be easily calculated based on the desired density requirements, making it an alternative solution.

We consider a typical *cellular topology* where the coordinates of the RP can be given as $\mathbf{o}_{m,m'}^{\rm uni}=\left(\sqrt{3}mL_\Delta, mL_\Delta+2m'L_\Delta, 0\right)$, where m and m' are integers with $-\frac{L}{L_\Delta}\le\sqrt{3}m\le\frac{L}{L_\Delta}$ and $-\frac{L}{L_\Delta}\le m+2m'\le\frac{L}{L_\Delta}$, and the spacing between RPs equals $2L_\Delta$. The codebook is constructed from the set of reflective patterns $\mathcal{U}_{\rm uni}=\{\boldsymbol{\theta}^*_{\mathbf{o}^{\rm uni}_{m,m'}}|\boldsymbol{\theta}^*_{\mathbf{o}^{\rm uni}_{m,m'}},\forall m,m'\}$, where $\boldsymbol{\theta}^*_{\mathbf{o}^{\rm uni}_{m,m'}}$ is obtained via (10) with respect to the locations $\mathbf{o}^{\rm uni}_{m,m'}$. The size of the codebook can be roughly calculated by taking the ratio of the indoor room area to the area of an individual hexagon, mathematically speaking, $\frac{4L^2}{3L_\Delta^2}$. The value of L_Δ plays a critical role in determining the coverage capability and indexing complexity of the codebook. It is evident that the optimal value of L_Δ falls within the range defined by (31) and (33). When L_Δ is set to a smaller value, the codebook size increases, leading to enhanced coverage capability. However, this also results in longer indexing time due to the larger number of available patterns. Conversely, selecting a larger L_Δ reduces the codebook size and indexing time, but it may compromise the coverage capability. Thus, the selection of L_Δ necessitates a careful trade-off between

[3]Alternatively, a similar approach could be applied to multi-user communication scenarios by controlling the overlap of adjacent coverage areas to a certain threshold. This can be achieved by dividing the RIS reflective units into groups, with each group dedicated to a specific user. This segmentation naturally minimizes interference among users in different coverage areas. However, implementing this strategy, involving RIS unit grouping and interference management, requires further investigation and is reserved for future research.

achieving sufficient coverage capability and maintaining reasonable indexing complexity.

2) Non-uniform topology: By utilizing the analytical results presented in **Section** III, the topology of RP locations can be optimized to improve the coverage capability.

Corollary 2 provides insight into the coverage area associated with each RP, which resembles an "elliptic-like" region. Based on this observation, we propose a topology where RPs are distributed on concentric circles with varying radii. These circles are centered at the origin $\mathbf{o}_o = (0,0,0)$, and the radii are determined by the major axis $k_v(k_{r_{\rm ru}}, \omega_{\max})$. The RP locations evenly spaced on each circle based on the minor axis $k_v(k_{r_{\rm ru}}, \omega_{\min})$.

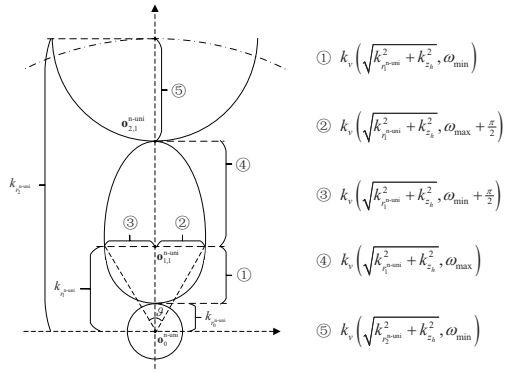

Fig. 5. The diagram depicts the placement of RPs and their associated coverage areas, delineated by solid lines based on a predefined threshold. To ensure coverage, it is important for adjacent areas to remain in proximity to each other.

We now calculate the location of the RPs for the non-uniform topology. Define $\mathbf{o}_0^{\text{n-uni}}$ as the RP at the origin point and $k_{r_0^{\text{n-uni}}} = k_v(k_{z_h}, \omega)$ as the corresponding coverage radius. In addition, let $\mathbf{o}_{i,j}^{\text{n-uni}}$ represents the location of the j-th RP on the i-th concentric circle, and $k_{r_{i,j}^{\text{n-uni}}}$ denote the corresponding distance to the origin point $(0,0,0)$. It follows that $k_{r_{i,j}^{\text{n-uni}}} = k_{r_i^{\text{n-uni}}}, \forall j$. We present the topology in **Algorithm 1**. As shown in Fig. 5, the RPs are distributed along the concentric circles represented by dashed lines, while the solid lines depict the coverage areas associated with each RP. In step 1), we establish the relationship between the radii of the concentric circles and the coverage distance and formulate $k_{r_i^{\text{n-uni}}}$ as a function of the coverage distance. In step 2), we calculate the number of RPs on the concentric circle with $\lceil\cdot\rceil$ representing the ceiling operation. To enhance the coverage, we introduce a density factor $\rho \in (0,1)$ to control the distribution density of the RPs. In step 3), we compute the locations of the RP $\mathbf{o}_{i,j}^{\text{n-uni}}$ by evenly distributing them on each concentric circle. We denote by $\mathcal{V}_{\text{n-uni}}$ the set of RP and by $\mathcal{U}_{\text{n-uni}}$ the corresponding codebook for the proposed the topology. Specifically, $\mathcal{V}_{\text{n-uni}} = \{\mathbf{o}_{i,j}^{\text{n-uni}} | \mathbf{o}_{i,j}^{\text{n-uni}}, \forall i,j\}$ and $\mathcal{U}_{\text{n-uni}} = \{\boldsymbol{\theta}_{\mathbf{o}_{i,j}^{\text{n-uni}}} | \boldsymbol{\theta}_{\mathbf{o}_{i,j}^{\text{n-uni}}}, \forall i,j\}$. The codebook size is $U_{\text{n-uni}} = |\mathcal{U}_{\text{n-uni}}|$. By adopting the non-uniform topology, the RPs are distributed in a denser manner in the center of the room, while being more sparsely placed towards the edges. This results in more efficient spatial sampling of the RPs, allowing for improved coverage with a reduced number of RPs and a smaller codebook size.

Algorithm 1 non-uniform topology

Initialization: γ, N, $k_{r_0^{\text{n-uni}}}$ and counters $i = 1, k = 1, j = 1$.

1) Compute the radius of each concentric circle

while $k_{r_i^{\text{n-uni}}} \le \sqrt{2}L$ **do**

if $i = 1$ **then**

Solve $k_{r_1^{\text{n-uni}}} : k_{r_1^{\text{n-uni}}} = k_{r_0^{\text{n-uni}}} + k_v\left(\sqrt{k^2_{r_1^{\text{n-uni}}} + k^2_{z_h}}, \omega_{\min}\right)$

else

Solve $k_{r_i^{\text{n-uni}}} : k_{r_i^{\text{n-uni}}} = k_{r_{i-1}^{\text{n-uni}}} + k_v\left(\sqrt{k^2_{r_{i-1}^{\text{n-uni}}} + k^2_{z_h}}, \omega_{\max}\right) + k_v\left(\sqrt{k^2_{r_i^{\text{n-uni}}} + k^2_{z_h}}, \omega_{\min}\right)$

end if

$i = i + 1, I = i - 1$

end while

2) Compute the number of RP on each concentric circle

for $k = 1 : I$ **do**

$$K_k = \rho \left\lceil \pi / \left(\tan^{-1} \frac{k_v\left(\sqrt{k^2_{r_k^{\text{n-uni}}}+k^2_{z_h}}, \omega_{\min}+\frac{\pi}{2}\right)}{k_{r_k^{\text{n-uni}}}} + \tan^{-1} \frac{k_v\left(\sqrt{k^2_{r_k^{\text{n-uni}}}+k^2_{z_h}}, \omega_{\max}+\frac{\pi}{2}\right)}{k_{r_k^{\text{n-uni}}}} \right) \right\rceil$$

end for

3) Compute the position of RP

for $k = 1 : I$ **do**

for $j = 1 : K_k$ **do**

$\mathbf{o}_{k,j}^{\text{n-uni}} = k_{r_k^{\text{n-uni}}}\left(\sin\frac{(j-1)\pi}{K_k}, \cos\frac{(j-1)\pi}{K_k}, 0\right)$

end for

end for

B. Feasibility of non-uniform topology

To ensure the feasibility of the proposed topology design, a crucial aspect is to demonstrate that the coverage areas corresponding to different RPs located on the same circumference are nearly equal.

According to expression (27), $J_{\mathbf{o}_{\rm u}}(N, \gamma_B, \gamma_C)$ is the only parameter that is not independent of the location when $k_{\rm ru}$ is fixed. More specifically, since $J_{\mathbf{o}_{\rm u}}(N, \gamma_B, \gamma_C)$ can be expanded as $J_{\mathbf{o}_{\rm u}}(N, \gamma_B, \gamma_C) = \left(\frac{\text{sinc}^{-1}\gamma_B}{N\pi}\right)^2 + \left(\frac{\text{sinc}^{-1}\gamma_C}{N\pi}\right)^2 + \frac{k^2_{r_{\rm ru}} - k^2_{z_h}}{4k^2_{r_{\rm ru}}} - \frac{k_{x_u}\text{sinc}^{-1}\gamma_B + k_{y_u}\text{sinc}^{-1}\gamma_C}{N\pi k_{r_{\rm ru}}}$, we note that only the last term changes with the location, and the maximum and the minimum value can be derived by solving the following problem $\mathcal{P}3$:

$$\mathcal{P}3: \max_{k_{x_u}, k_{y_u}} \pm\left(k_{x_u}\text{sinc}^{-1}\gamma_B + k_{y_u}\text{sinc}^{-1}\gamma_C\right) \quad (34a)$$

$$\text{s.t. } k^2_{x_u} + k^2_{y_u} = k^2_{\rm ru}. \quad (34b)$$

Applying the Lagrange multipliers method, and we can show that the objective fucntion reaches the limit $\pm k_{\rm ru}\sqrt{\text{sinc}^{-2}\gamma_B + \text{sinc}^{-2}\gamma_C}$ if and only if $\{k_{x_u}, k_{y_u}\} = \pm\frac{k_{\rm ru}}{\sqrt{\text{sinc}^{-2}\gamma_B + \text{sinc}^{-2}\gamma_C}}\left\{\text{sinc}^{-1}\gamma_B, \text{sinc}^{-1}\gamma_C\right\}$. Furthermore, due to the monotonically decreasing nature of $\text{sinc}^{-1}(\cdot)$ in the range $[0,1]$, it is not possible for both $\text{sinc}^{-1}\gamma_B$ and $\text{sinc}^{-1}\gamma_C$ to reach their maximum values simultaneously, as they are subject to the constraint $\gamma = \gamma_B\gamma_C$. We hence have $\sqrt{\text{sinc}^{-2}\gamma_B + \text{sinc}^{-2}\gamma_C} < \sqrt{2}\text{sinc}^{-1}\gamma$. In addition, in order to maintain stability in service quality, it

is common to set the channel gain threshold γ to be close to 1, for example, $\gamma \geq 0.8$. Recalling $J_{\mathbf{o}_\mathrm{u}}(N,\gamma_B,\gamma_C)$ and substituting $\mathrm{sinc}^{-1}0.8 \approx 0.36\pi$ into it, we observe that $\max\{J_{\mathbf{o}_\mathrm{u}}(N,\gamma_B,\gamma_C)\} - \min\{J_{\mathbf{o}_\mathrm{u}}(N,\gamma_B,\gamma_C)\} < \frac{1}{N}$. Due to the large number of units equipped on the RIS, the variation of $J_{\mathbf{o}_\mathrm{u}}(N,\gamma_B,\gamma_C)$ is relatively small. This observation suggests that the major and minor axes of the coverage outlined by $k_v(k_{r_\mathrm{ru}},\omega)$ are approximately equal with a fixed k_ru, validating the feasibility of the proposed topology design.

C. Coverage probability

The coverage probability is a crucial metric for evaluating the effectiveness of a topology approach. However, determining the exact coverage of the non-uniform topology in this paper presents challenges. This is because the coverage area corresponding to each RP is "ellipse-like" rather than an ellipse, as described in *Remark* 2, making its calculation complex. Nevertheless, leveraging its "ellipse-like" property, we can approximate the coverage ratio assuming the ellipse coverage, as demonstrated in the following remark.

Remark 3: Based on the non-uniform topology of RP obtained by **Algorithm 1**, the coverage probability with channel gain not less than $\frac{\gamma N^2}{4r_0^2}$ can be approximated as

$$\begin{aligned}&\mathbb{P}\left(\tilde{\mathcal{G}}_{\tilde{\mathbf{o}}_\mathrm{u}}\left(\theta^*_{\mathbf{o}_\mathrm{u}}\right) \geqslant \frac{\gamma N^4}{4r_0^2}\right)\\ &\approx \frac{k^2_{r_0^{\text{n-uni}}} + \sum\limits_{k=1}^{I} K_k E\left(k_{r_{\mathrm{ru},k}^{\text{n-uni}}}\right)\sqrt{k_{r_{\mathrm{ru},k}^{\text{n-uni}}} - \frac{k^2_{z_h}}{1-4J_{\mathbf{o}_\mathrm{u}}(N,\gamma_B,\gamma_C)}}}{\left(k_{r_I^{\text{n-uni}}} + k_v\left(k_{r_{\mathrm{ru},I}^{\text{n-uni}}},\omega_{\max}\right)\right)^2},\end{aligned} \tag{35}$$

where I is the number of concentric circles, $k_{r_{\mathrm{ru},k}^{\text{n-uni}}} = \sqrt{k^2_{r_k^{\text{n-uni}}} + k^2_{z_h}}$ represents the distance between the RIS to the k-th concentric circle.

Proof: Utilize the equation for the area of an ellipse: $S = \pi ab$, where a and b are the lengths of the semi-major and semi-minor axes of the ellipse, respectively. We compute the sum of the coverage areas of all RPs corresponding to channels with gains not less than $\frac{\gamma N^2}{4r_0^2}$, and the overall area, i.e., the area of a circle centered at $\mathbf{o}_\mathrm{o}$ with the farthest end of the coverage corresponding to the outermost RP as its radius. The ratio of these areas can then be approximated as the coverage of the non-uniform topology. ■

D. Indexing Method

While a brute-force search of the codebook can identify the optimal RIS reflective pattern for any location in the room, this approach is computationally demanding and can exceed the time required for channel estimation, even with a non-uniform topology. To overcome this issue, we introduce a transmission protocol and an indexing method designed to efficiently locate the optimal RIS reflective pattern, meeting the low-latency requirement.

The proposed transmission protocol can be found in Fig. 1(a). To be more specific, during the access phase, the AP identifies the optimal reflective pattern from the codebook $\mathcal{U}_{\text{n-uni}}$ using an efficient indexing method, while in the tracking phase, the AP switches the reflective pattern according to the movement of the UE.

1) Access Stage: Given the absence of CSI at the AP and the knowledge of the UE's location, we propose a two-step searching method that utilizes the location-based codebook. The search procedure follows a "rough-exact selection" strategy, which involves three steps:

- Offline pre-process: Generating a "head codebook" $\mathcal{U}_\mathrm{h}$ comprising T_h pre-selected reflective patterns whose corresponding RPs are the centers of subareas within the room. To achieve this, we first divide the codebook $\mathcal{U}_{\text{n-uni}}$ into T_h sub-codebooks utilizing the *Same-size K-means*[4] algorithm, which groups reflective patterns according to their corresponding RP locations. Each sub-codebook $\mathcal{U}_{\text{n-uni},t}, \forall t$ comprises $U_\text{sub} = U_{\text{n-uni}}/T_\mathrm{h}$ adjacent RPs. The set $\mathcal{V}_{\text{n-uni},t}$ represents the RP locations within the tth sub-codebook. The tth sub-codebook, denoted as $\mathcal{U}_{\text{n-uni},t}$, is obtained by selecting codewords in $\mathcal{U}_{\text{n-uni}}$ whose corresponding RP locations belong to $\mathcal{V}_{\text{n-uni},t}$. Mathematically, this can be expressed as $\mathcal{U}_{\text{n-uni},t} = \{\boldsymbol{\theta}_{\mathbf{o}_{i,j}^{\text{n-uni}}} | \mathbf{o}_{i,j}^{\text{n-uni}} \subset \mathcal{V}_{\text{n-uni},t}\}$. In this manner, the indoor coverage area is partitioned into T_h regions.
  Then, for each region, we select the reflective pattern from the corresponding sub-codebook that corresponds to the RP closest to the center of the region as the pre-selected reflective pattern in $\mathcal{U}_\mathrm{h}$, i.e., $\mathcal{U}_\mathrm{h} = \{\boldsymbol{\theta}_{\mathbf{o}_t} | \boldsymbol{\theta}_{\mathbf{o}_{i^*,j^*}^{\text{n-uni},t}}, \forall t\}$ with
  $$\mathbf{o}_{i^*,j^*}^{\text{n-uni},t} = \arg\min_{i,j} \left\| \mathbf{o}_{i,j} - \tfrac{1}{U_t}\sum\nolimits_{i,j} \mathbf{o}_{i,j}^{\text{n-uni}} \right\|, \tag{36}$$
  with $\mathbf{o}_{i,j}^{\text{n-uni}} \subset \mathcal{V}_{\text{n-uni},t}, \forall t$. The procedure of "offline pre-process" is summarized in **Algorithm** 2.
- Rough selection: In this stage, the UE at $\mathbf{o}_\mathrm{u}$ transmits a pilot sequence of length T_h, while the RIS switches the pre-selected reflective patterns in $\mathcal{U}_\mathrm{h}$ at each pilot symbol, mathematically speaking, the t-th received pilot symbol can be given by
  $$r_{\mathbf{o}_\mathrm{u}}(\boldsymbol{\theta}_{\mathbf{o}_t}) = z_{\mathbf{o}_\mathrm{u}}(\boldsymbol{\theta}_{\mathbf{o}_t})\, s_t + w_t, \;\; \boldsymbol{\theta}_{\mathbf{o}_t} \subset \mathcal{U}_\mathrm{h}. \tag{37}$$
  The strength of the received T_h pilots is measured at the AP. The sub-codebook with the highest power reflective pattern is identified, and its corresponding region is selected as the search space for the "exact selection" stage, i.e., $\mathcal{U}_{\text{n-uni},t^*}$ with $t^* = \arg\max_t \left| r_{\mathbf{o}_\mathrm{u}}(\boldsymbol{\theta}_{\mathbf{o}_t}) \right|^2$.
- Exact selection: In this stage, the UE transmits a pilot sequence of length U_sub, while the RIS configures itself with the reflective patterns in the sub-codebook $\mathcal{U}_{\text{n-uni},t^*}$. The reflective pattern with the highest received power is then selected for transmission, i.e., $\boldsymbol{\theta}_{\mathbf{o}_{i^*,j^*}^{\text{n-uni}}} = \arg\max_{i,j} \left| r_{\mathbf{o}_\mathrm{u}}(\boldsymbol{\theta}_{\mathbf{o}_{i,j}^{\text{n-uni}}}) \right|^2$, $\boldsymbol{\theta}_{\mathbf{o}_{i,j}^{\text{n-uni}}} \subset \mathcal{U}_{\text{n-uni},t^*}$.

2) Tracking stage: As the UE moves, the initially selected reflective pattern for the access stage may become mismatched, resulting in degraded performance. To maintain the quality of services, it is necessary to periodically update the reflective pattern to adapt to the UE's new location.

[4]Please refer to [44] for further details.

Algorithm 2 Generate $\mathcal{U}_{\text{n-uni},t}$ and $\mathcal{U}_{\text{h}}$

Initialization: $\mathcal{V}_{\text{n-uni}}$, $\mathcal{U}_{\text{n-uni}}$, $\mathcal{U}_{\text{h}} = \emptyset$, and number of clusters T_{h}

1) Run *Same-size K-means* with input $\mathcal{V}_{\text{n-uni}}$ and T_{h}, and output $\{\mathcal{V}_{\text{n-uni},t}\}_{t=1,\ldots,T_{\text{h}}}$, $\{\mathcal{U}_{\text{n-uni},t}\}_{t=1,\ldots,T_{\text{h}}}$

2) Find the RP closest to the centroid of each sub-cluster via (36)

3) Generate $\mathcal{U}_{\text{h}}$: $\mathcal{U}_{\text{h}} = \mathcal{U}_{\text{h}} \cup \boldsymbol{\theta}_{\mathbf{o}_{i^*,j^*}^{\text{n-uni},t}}, \forall t$

During the tracking phase, the selection of the reflective pattern becomes simpler since the previously selected reflective pattern in the access stage provides an estimate of the UE's position. Therefore, the AP only needs to consider the reflective patterns whose corresponding RPs surround the UE's position and select the optimal reflective pattern from among them. This process can be repeated periodically to track the UE's movement and update the reflective pattern selection. The entire procedure can be summarised as:

- At each time slot during the tracking phase, the AP generates a candidate reflective pattern set $\mathcal{U}_{\text{tr}}$, which consists of T_{tr} reflective patterns. These reflective patterns are chosen based on their corresponding RPs, which surround the RP $\mathbf{o}_{i^*,j^*}^{\text{n-uni}}$ that was selected in the previous time slot. The set $\mathcal{U}_{\text{tr}}$ includes $\boldsymbol{\theta}_{\mathbf{o}_{i^*,j^*}^{\text{n-uni}}}$ as one of the reflective patterns.
- Similar to the transmission protocol at *Access Stage*, the UE sends a pilot sequence of length T_{tr}, while the RIS traverses the reflective patterns in $\mathcal{U}_{\text{tr}}$ at each pilot symbol correspondingly.
- The reflective pattern with the highest received power is selected as the RP for the current time slot.

Based on the designs of *Access Stage* and *Tracking Stage*, we have developed a transmission protocol as illustrated in Fig. 5. This protocol requires a pilot overhead of $T_{\text{h}} + U_{\text{sub}}$ for the time slot at the *Access Stage*, and T_{tr} per time slot at the *Tracking Stage*. More precisely, since $U_{\text{n-uni}} = T_{\text{h}} \times U_{\text{sub}}$, we simply have inequality $T_{\text{h}} + U_{\text{sub}} \geq 2\sqrt{U_{\text{n-uni}}}$, with equality holding if and only if $T_{\text{h}} = U_{\text{sub}} = \sqrt{U_{\text{n-uni}}}$. Hence, to achieve minimum overhead, the value of T_{h} should be chosen around $\sqrt{U_{\text{n-uni}}}$. On the other hand, the value of T_{tr} typically depends on the specific topology of the environment. For the uniform topology considered in this paper, $T_{\text{tr}} = 7$. In a non-uniform topology, the density of RPs varies across different locations, with a higher concentration of RPs in the center of the house. As a result, the value of T_{tr} is influenced by the distribution of RPs, as it needs to account for the denser RP deployment in the central area of the house.

It is evident that both the access and tracking phases offer substantial reductions in pilot and RIS optimization overheads compared to CE-based transmission protocols, where the CE overhead scales with the number of reflective units in the RIS. However, in multiuser communication scenarios, this approach can pose challenges, as the spatial combinations needed to match the codebook increase geometrically, significantly impacting searching efficiency. This issue can potentially be addressed through RIS clustering and UE association techniques, which are beyond the scope of this paper.

E. Spectral efficiency

We investigate the uplink throughput of the proposed transmission protocol. Unlike conventional transmission protocols, where the channel estimation overhead is lower bounded by the number of reflective units on the RIS (N^2), the pilot overhead required for the proposed location-based PB-based transmission protocol remains constant regardless of the RIS. Specifically, the pilot overhead is lower bounded by $2\sqrt{U_{\text{n-uni}}}$ for the access phase and T_{tr} for the tracking phase.

Denoting $\tilde{\mathbf{o}}_{\text{u}}(j)$ as the location of the UE and $\boldsymbol{\theta}_{\mathbf{o}_{\text{u}}}^*(j)$ as the selected reflective pattern at the j-th time slot during the transmission time J, the average uplink SE (in bit/s/Hz) during J time slots for the proposed protocol is given by

$$\bar{R} = \frac{1}{J}\left(R_{\text{ac}}(1) + \sum\nolimits_{j=2}^{J} R_{\text{tr}}(j)\right), \tag{38}$$

where $R_{\text{ac}}(1)$ and $R_{\text{tr}}(j)$ represent the achievable SE for the access phase and the tracking phase, and are given by

$$\begin{aligned} R_{\text{ac}}(1) &= \tfrac{V_{\max} - 2\sqrt{U_{\text{n-uni}}}}{V_{\max}} \log_2\left(1 + \mathcal{G}_{\tilde{\mathbf{o}}_{\text{u}}(1)}\left(\boldsymbol{\theta}_{\mathbf{o}_{\text{u}}}^*(1)\right)/\sigma^2\right), \\ R_{\text{tr}}(j) &= \tfrac{V_{\max} - T_{\text{tr}}}{V_{\max}} \log_2\left(1 + \mathcal{G}_{\tilde{\mathbf{o}}_{\text{u}}(j)}\left(\boldsymbol{\theta}_{\mathbf{o}_{\text{u}}}^*(j)\right)/\sigma^2\right) \end{aligned} \tag{39}$$

where $V_{\max}$ is the overall number of symbols transmitted in one slot. Regarding the conventional protocol, channel estimation allows the RIS to adaptively configure itself in a real-time manner, and the average achievable SE can be calculated as follows:

$$\bar{R}_{\text{con}} = \tfrac{V_{\max} - N^2}{J V_{\max}} \sum_{j=1}^{J} \log_2\left(1 + \mathcal{G}_{\tilde{\mathbf{o}}_{\text{u}}(j)}\left(\boldsymbol{\theta}_{\tilde{\mathbf{o}}_{\text{u}}}^*(j)\right)/\sigma^2\right), \tag{40}$$

where $\boldsymbol{\theta}_{\tilde{\mathbf{o}}_{\text{u}}}^*(j)$ is the real-time optimal reflective pattern configured for the UE at $\tilde{\mathbf{o}}_{\text{u}}(j)$.

V. Numerical Results

In our paper, we consider an indoor scenario with $L = 10$. A UPA-type RIS is hanging on the center of the roof, consisting of $N \times N$ elements.

In Fig. 6, we verify the theoretical results of the channel gain w.r.t the number of the reflective units on the RIS. We randomly select a location $\mathbf{o}_{\text{u}}$ in the room as the target location and compute the channel gain using the optimal reflective pattern $\boldsymbol{\theta}_{\mathbf{o}_{\text{u}}}^*$. Considering that the real propagation environment may be more complex, we simulate the channel gain of the Rician channel with unknown NLoS CSI, where the Rician factor is set to 6 dB [42]. It is intuitive that the theoretical result in *Proposition 1* closely matches the numerical simulation results. This demonstrates the feasibility and accuracy of the approximations used in Appendix A. In addition, we observe a small discrepancy between the approximation and simulations when the number of units is less than 10, which is attributed to the neglect of the channel gain contributed by the non-tunable part b. As the number of elements increases, the channel gain from the tunable part becomes dominant, resulting in a "perfect" match between the theoretical and numerical channel gains. More importantly, the attenuation due to unknown NLoS

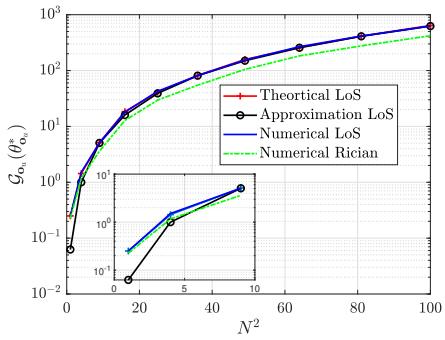

Fig. 6. The comparison of theoretical channel gain, approximation, and simulations for LoS and Rician channels w.r.t the number of antennas.

CSI in comparison to the Rician case is relatively minor and does not significantly alter the channel gain trend.

The accuracy of the theoretical channel gain to the real channel gain is demonstrated in Fig. 7 when location offset exists. We compare the NMSE of the channel gain to the different RPs with varying distances k_v, where NMSE is defined as NMSE $= \frac{\left\|\mathcal{G}_{\mathbf{o}_{\tilde{\mathrm{u}}}}(\boldsymbol{\theta}^*_{\mathbf{o}_{\mathrm{u}}}) - \mathcal{G}_{\mathbf{o}_{\tilde{\mathrm{u}}}}(\boldsymbol{\theta}^*_{\mathbf{o}_{\mathrm{u}}})\right\|^2}{\left\|\mathcal{G}_{\mathbf{o}_{\tilde{\mathrm{u}}}}(\boldsymbol{\theta}^*_{\mathbf{o}_{\mathrm{u}}})\right\|^2}$. Firstly, it can be observed that if the distance between the RP and the origin point in the xy-plane is less than $40\,\lambda$, the theoretical results closely match the simulations, even when k_v increases beyond $50\,\lambda$. However, as the RP gradually moves away from the center of the room, the theoretical channel gain starts to deviate from the actual channel gain. For instance, at a distance of $100\,\lambda$ from the center of the room, the NMSE increases to 0.08 at a distance of $30\,\lambda$ from the RP, and eventually reaches 0.16 with a distance exceeding $50\,\lambda$.

Fig. 8 illustrates the uniform topology and the proposed non-uniform topology of the RPs. In contrast to the uniform topology, the non-uniform topology features a higher density of RPs in the central area of the room, while the density decreases significantly towards the corners of the room. This approach takes advantage of the characteristic that the channel gain decreases more rapidly in the near-field and more slowly in the far-field. As a result, the proposed non-uniform topology ensures better uniform coverage in the central area, as demonstrated in Fig. 9. As expected, the uniform topology exhibits a

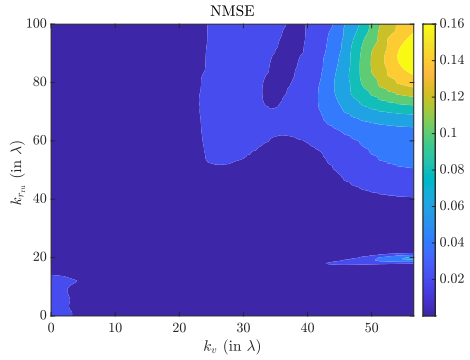

Fig. 7. The NMSE of theoretical approximated channel gain with different k_v for RPs at different locations.

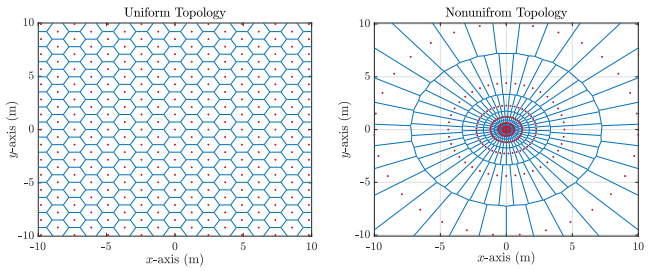

Fig. 8. The comparison of uniform RP topology and non-uniform RP topology.

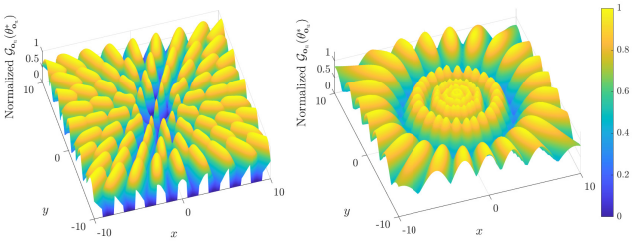

Fig. 9. The normalized channel gain for uniform RP topology and non-uniform RP topology given by Fig. 8.

coverage gap in the central area. While the coverage capability in the edge of the room is comparatively worse under the non-uniform topology than under the uniform topology, it remains acceptable as long as it meets the predetermined lower limit. This trade-off allows for a reduction in the codebook size.

In Fig. 10, the coverage probability of two different topologies with varying numbers of RPs is depicted. The number of RPs (say the density of RPs) is adjusted by modifying the distance L_Δ for the uniform topology, and by varying the density factor ρ for the non-uniform topology. From the figure, it is evident that the non-uniform topology outperforms the uniform topology in terms of coverage. For instance, achieving 80 % of the performance using the optimal reflective pattern requires approximately 250 RPs with non-uniform topology, whereas it necessitates around 300 RPs for uniform topology. Furthermore, with the non-uniform topology, the channel gain performance hardly drops below 50 % of that using the optimal reflective pattern, ensuring the robustness of the PB-based protocol.

After demonstrating the advantage of the non-uniform topology in terms of coverage, we now evaluate the performance of the proposed transmission protocol. In Fig. 11, we consider a non-uniform topology of representative points and assume a random UE location. The communication lasts for 1000 s while the UE moves at a speed of 2 m/s in a random direction during the connection. We compare the CDF of the channel gain during the connections using different values of T_{tr} in the tracking stage. The CDF for the benchmark case of uniform topology with $T_{\mathrm{tr}} = 7$ is also included for comparison. Firstly, we observe that the coverage probability improves as T_{tr} increases for the non-uniform topology. This can be attributed to the distribution of RPs. During the tracking phase, the set of T_{tr} candidate reflective patterns is selected based on the RPs surrounding the previously selected RP. Due to the dense

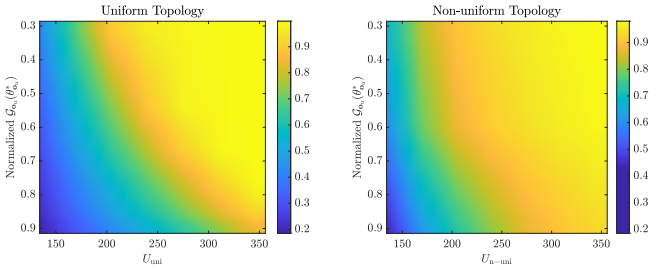

Fig. 10. The coverage probability for uniform topology and non-uniform topology with different density of RPs.

deployment of RPs in the central region, the area covered by the set of candidate reflective patterns becomes very small. As a result, the distance moved by the UE per time slot is larger than the area covered by the candidate set, causing the optimal reflective pattern to be non-existent in the candidate set. This leads to a bias in all subsequent tracking. Moreover, it can be observed that the performance with $T_{\text{tr}} = 16$ approaches that of the brute-force searching method, where $T_{\text{tr}} = U_{\text{n-uni}}$, indicating the feasibility of the tracking method. In contrast, with uniform deployment, the area covered by the RPs corresponding to $T_{\text{tr}} = 7$ candidate reflective patterns is sufficiently large, making it difficult to lose track. However, due to the poor coverage probability, the performance with uniform topology fails to meet the requirements.

We compare the average achievable SE of the proposed transmission protocols concerning pilot length for different topologies in the LoS and Rician scenarios in Fig. 12(a) and Fig. 12(c), respectively. In this comparison, we set the Rician factor to 6 dB, and the NLoS CSI is unknown. For the uniform topology, increasing the pilot length T_{tr} does not enhance tracking accuracy, resulting in $T_{\text{tr}} = 7$ offering optimal achievable SE as a benchmark. Conversely, the pilot length T_{tr} significantly influences tracking accuracy for the non-uniform topology, affecting achievable SE accordingly. An important observation is that the average achievable SE for the non-uniform topology with the proposed transmission protocol peaks at $T_{\text{tr}} = 16$. Comparing Fig. 12(a) and Fig. 12(c), we note a notable performance improvement in the conventional transmission protocol, attributed to channel estimation to capture NLoS CSI, thereby enhancing RIS optimization

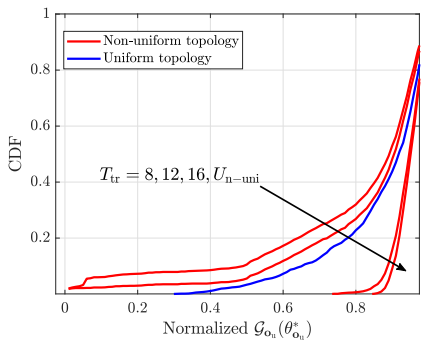

Fig. 11. The CDF of the normalized channel gain for non-uniform topology with different T_{tr}.

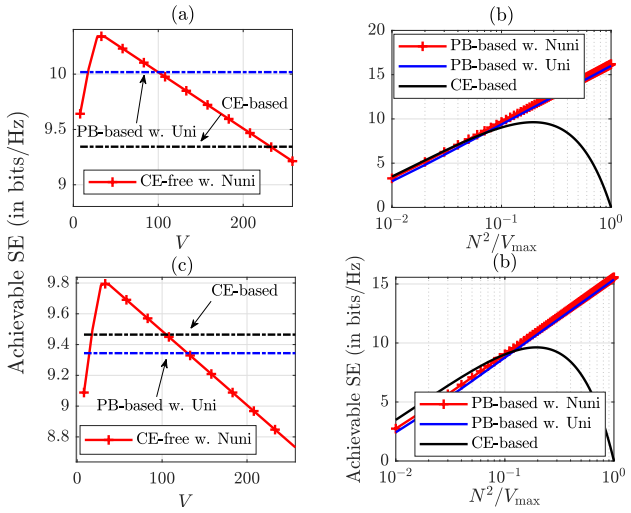

Fig. 12. The comparison of average achievable SE with conventional protocol and PB-based protocol, where (a) and (c) show the achievable SE w.r.t the pilot length with fixed $N = 10$ for LoS and Rician channel, respectively; (b) and (d) show the achievable SE w.r.t the number of RIS unit for LoS and Rician channel, respectively.

performance—a capability lacking in the PB-based strategy. Fig. 12(b) and Fig. 12(d) illustrate the achievable SE concerning the ratio between the number of elements of the RIS and $V_{\max}$ for LoS and Rician channels, respectively. Notably, the pilot overhead required for the proposed tracking protocol remains constant regardless of the number of RIS elements N^2, leading to a monotonic improvement in achievable SE with an increasing number of RIS elements. Furthermore, the performance of the conventional transmission protocol surpasses that of the proposed transmission protocol only when N is small. However, this advantage diminishes due to the limited channel gain achieved by a small number of reflective elements. As the number of elements increases, the pilot overhead required for the conventional transmission protocol with channel estimation becomes a limiting factor, resulting in a significant decline in achievable SE. This challenge persists even with Rician channels, underscoring the impact of overhead. From another perspective, this highlights the potential of leveraging prior knowledge of location-based CSI to reduce system overhead and enhance performance.

VI. Conclusion

In this paper, we proposed a PB-based transmission protocol to reduce pilot consumption in RIS-assisted indoor systems. By exploiting the stable indoor propagation environment, we first evaluated a theoretical approximation of the channel gain based on the location. Using this approximation, we constructed a reflective pattern codebook that corresponds to the coverage areas indicated by the theoretical results. A transmission protocol is hence proposed where the channel estimation phase is replaced by the codebook indexing. We designed different indexing strategies for the access phase and tracking phase of the protocol, resulting in significantly lower pilot overhead compared to the conventional transmission protocol. The numerical simulation validated the accuracy of

our theoretical channel gain approximation and verified the coverage of the reflective pattern codebook. More importantly, benefiting from the reduced pilot consumption, the simulation demonstrated that the proposed transmission protocol achieves higher achievable SE compared to the conventional transmission protocol.

APPENDIX A
PROOF OF PROPOSITION 1

To evaluate the channel gain, we first introduce a lemma that demonstrates the result of the sum of exponential functions of angles in an arithmetic series.

Lemma 1: Given a $1 \times K$ steering vector $\mathbf{s} = [e^{-j(a+b)}, e^{-j(a+2b)}, \ldots, e^{-j(a+Kb)}]$ with a and b being two arbitrary values, we have

$$\mathbf{s1}^T = \tfrac{\sin(Kb/2)}{\sin(b/2)} e^{-j\left(a+\frac{1}{2}(K+1)b\right)}. \tag{41}$$

Proof: With the definition of $\mathbf{s}$, we arrive at

$$\begin{aligned}\mathbf{s1}^T &= \sum\nolimits_{k=1}^{K} e^{-j(a+kb)} \\ &= \sum\nolimits_{k=1}^{K} \cos(a+kb) - i\sum\nolimits_{k=1}^{K} \sin(a+kb). \end{aligned}\tag{42}$$

Let us first compute the real part of (42). According to the trigonometric identities, we observe

$$\begin{aligned}&\sin\tfrac{b}{2}\sum\nolimits_{k=1}^{K}\cos(a+kb) \\ &= \tfrac{1}{2}\sum\nolimits_{k=1}^{K}\sin\left(a+\tfrac{(2k+1)b}{2}\right) - \sin\left(a+\tfrac{(2k-1)b}{2}\right) \\ &= \tfrac{1}{2}\left(\sin\left(a+\tfrac{(2K+1)b}{2}\right) - \sin\left(a+\tfrac{b}{2}\right)\right) \\ &= \cos\left(a+\tfrac{1}{2}(K+1)b\right)\sin\left(\tfrac{Kb}{2}\right), \end{aligned}\tag{43}$$

and hence we get

$$\sum\nolimits_{k=1}^{K}\cos(a+kb) = \tfrac{\sin(Kb/2)}{\sin(b/2)}\cos\left(a+\tfrac{1}{2}(K+1)b\right). \tag{44}$$

Similarly, the imagery part of (42) equals to

$$\sum\nolimits_{k=1}^{K}\sin(a+kb) = \tfrac{\sin(Kb/2)}{\sin(b/2)}\sin\left(a+\tfrac{1}{2}(K+1)b\right), \tag{45}$$

and combining (44) and (45) we complete the proof. ■

We now compute b using *Lemma 1*. Recall the location of UE, AP, and the RIS, and substituting (2) and (3) into b, we arrive at

$$\begin{aligned}b = \sum\nolimits_{n=1}^{N}\sum\nolimits_{n'=1}^{N} &e^{-j2\pi\sqrt{\left(k_{x_u}-\frac{n-1}{2}\right)^2+\left(k_{y_u}-\frac{n'-1}{2}\right)^2+k_{z_h}^2}} \\ &\times e^{-j2\pi\sqrt{k_L-\left(\frac{n-1}{2}\right)^2+\left(k_L-\frac{n'-1}{2}\right)^2}}\end{aligned}\tag{46}$$

It is rather challenging to gain insights from the given expression directly. To address this, we utilize the Taylor polynomials of a function of two variables

$$\begin{aligned}f(x,y) &= \sqrt{x^2+y^2+c_1x+c_2y+c_3} \\ &\approx \sqrt{c_3} + \tfrac{c_1}{2\sqrt{c_3}}x + \tfrac{c_2}{2\sqrt{c_3}}y, \end{aligned}\tag{47}$$

and select the first order w.r.t $n-1$ and $n'-1$ to simplify the expression:

$$\begin{aligned}k_{r_{\mathrm{ru},n,n'}} &= \sqrt{\left(k_{x_u}-\tfrac{n-1}{2}\right)^2+\left(k_{y_u}-\tfrac{n'-1}{2}\right)^2+k_{z_h}^2} \\ &\approx k_{r_{\mathrm{ru},1,1}} + \tfrac{k_{x_u}+k_{y_u}}{2k_{r_{\mathrm{ru},1,1}}} - \tfrac{k_{x_u}}{2k_{r_{\mathrm{ru},1,1}}}n - \tfrac{k_{y_u}}{2k_{r_{\mathrm{ru},1,1}}}n', \end{aligned}\tag{48}$$

$$\begin{aligned}k_{r_{\mathrm{ar},n,n'}} &= \sqrt{\left(k_L-\tfrac{n-1}{2}\right)^2+\left(k_L-\tfrac{n'-1}{2}\right)^2} \\ &\approx \sqrt{2}k_L + \tfrac{1}{\sqrt{2}} - \tfrac{1}{2\sqrt{2}}n - \tfrac{1}{2\sqrt{2}}n'. \end{aligned}\tag{49}$$

Substituting (48) and (49) into (46) and after some manipulations, we obtain

$$b \approx \sum\nolimits_{n=1}^{N}\sum\nolimits_{n'=1}^{N} e^{-j\left(A^*+B^*n+C^*n'\right)}. \tag{50}$$

Using *Lemma 1* w.r.t n and n' respectively, we obtain that

$$b = f(B^*)f(C^*)e^{-j\left(A^*+\frac{N+1}{2}(B^*+C^*)\right)}. \tag{51}$$

Hence, we have

$$\begin{aligned}\tau &= h_{\mathrm{d}} + \tfrac{b}{2r_0} \\ &= e^{-j\kappa r_{\mathrm{au}}} + \tfrac{f(B^*)f(C^*)}{2r_0}e^{-j\left(A^*+\frac{N+1}{2}(B^*+C^*)\right)} \\ &= \cos(\kappa r_{\mathrm{au}}) + \tfrac{f(B^*)f(C^*)}{2r_0}\cos\left(A^*+\tfrac{N+1}{2}(B^*+C^*)\right) \\ &- j\left(\sin(\kappa r_{\mathrm{au}}) + \tfrac{f(B^*)f(C^*)}{2r_0}\sin\left(A^*+\tfrac{N+1}{2}(B^*+C^*)\right)\right) \\ &= \Big(1+\tfrac{f(B^*)^2f(C^*)^2}{4r_0^2} \\ &\quad + \tfrac{f(B^*)f(C^*)}{r_0}\cos\left(A^*+\tfrac{N+1}{2}(B^*+C^*)-\kappa r_{\mathrm{au}}\right)\Big)^{\frac{1}{2}} \\ &\times e^{-j\left(\operatorname{atan}\frac{\sin(\kappa r_{\mathrm{au}})+\frac{f(B^*)f(C^*)}{2r_0}\sin\left(A^*+\frac{N+1}{2}(B^*+C^*)\right)}{\cos(\kappa r_{\mathrm{au}})+\frac{f(B^*)f(C^*)}{2r_0}\cos\left(A^*+\frac{N+1}{2}(B^*+C^*)\right)}\right)}. \end{aligned}\tag{52}$$

Regarding $c_{n,n'}^*$, since $c_{n,n'}^*, \forall n, n'$ have the same phase equaling to φ_τ, we therefore have

$$\begin{aligned}&\sum\nolimits_{n=1}^{N}\sum\nolimits_{n'=1}^{N} c_{n,n'}^* \\ &= N^2 e^{-j\left(\operatorname{atan}\frac{\sin(\kappa r_{\mathrm{au}})+\frac{f(B^*)f(C^*)}{2r_0}\sin\left(A^*+\frac{N+1}{2}(B^*+C^*)\right)}{\cos(\kappa r_{\mathrm{au}})+\frac{f(B^*)f(C^*)}{2r_0}\cos\left(A^*+\frac{N+1}{2}(B^*+C^*)\right)}\right)},\end{aligned}\tag{53}$$

whose channel gain equals N^2 and thus completes the proof.

APPENDIX B
PROOF OF PROPOSITION 2

Similar to *Proposition 1*, we first evaluate the non-tunable part with a given RIS profile $\boldsymbol{\theta}_{\mathbf{o}_{\mathrm{u}}}^*$ at location $\mathbf{o}_{\tilde{\mathrm{u}}}$.

Substituting $\tilde{h}_{n,n'}$ into $\tilde{b}$, we obtain

$$\tilde{b} = \sum\nolimits_{n=1}^{N}\sum\nolimits_{n'=1}^{N} e^{-j2\pi\left(k_{r_{\mathrm{br},n,n'}}+k_{\tilde{r}_{\mathrm{ru},n,n'}}\right)}. \tag{54}$$

Utilizing Taylor polynomials as demonstrated in the proof of

Proposition 1, we approximate $k_{\tilde{r}_{\mathrm{ru},n,n'}}$ as

$$\begin{aligned} k_{\tilde{r}_{\mathrm{ru},n,n'}} &= \sqrt{\left(k_{\tilde{x}_u} - k_{x_{r,n,n'}}\right)^2 + \left(k_{\tilde{y}_u} - k_{y_{r,n,n'}}\right)^2 + k_{z_h}^2} \\ &\approx \tfrac{k_{\tilde{y}_u} - k_{y_u}}{2f(k_v,\omega)} n' + \tfrac{k_{\tilde{x}_u} - k_{x_u}}{2f(k_v,\omega)} n + f\left(k_v,\omega\right) + \tfrac{k_{x_u} + k_{y_u} - k_{\tilde{x}_u} - k_{\tilde{y}_u}}{2f(k_v,\omega)}, \end{aligned} \tag{55}$$

where

$$f\left(k_{r_{\mathrm{ru}}}, k_v, k_u(\omega)\right) \overset{(a)}{=} \sqrt{k_{r_{\mathrm{ru}}}^2 + k_v^2 - 2k_v k_u(\omega)}, \tag{56}$$

where (a) is obtained using $k_{x_u}\sin\omega + k_{y_u}\cos\omega = \sqrt{k_{x_u}^2 + k_{y_u}^2}\sin(\omega + \tan^{-1}\frac{k_{y_u}}{k_{x_u}})$. Together with (49) and using *Lemma 1*, we arrive

$$\begin{aligned} \tilde{b} &\approx \sum\nolimits_{n=1}^{N}\sum\nolimits_{n'=1}^{N} e^{-j\left(\bar{A} + \bar{B}n + \bar{C}n'\right)} \\ &= \frac{\sin\left(N\bar{B}/2\right)\sin\left(N\bar{C}/2\right)}{\sin\left(\bar{B}/2\right)\sin\left(\bar{C}/2\right)} e^{-j\left(\bar{A} + \frac{N+1}{2}\left(\bar{B}+\bar{C}\right)\right)}. \end{aligned} \tag{57}$$

Now, we compute the channel gain of the tunable terms. Since the reflective coefficient of the (n,n')th element is optimized for the cascaded channel $a_{n,n'}$, the phase then equals $\theta^*_{\mathbf{o}_\mathrm{u},n,n'} = \varphi_{a_{n,n'}} - \varphi_b$. The overall channel of the tunable part can be represented as

$$\begin{aligned} &\sum\nolimits_{n=1}^{N}\sum\nolimits_{n'=1}^{N} \tilde{a}_{n,n'} e^{j\theta^*_{\mathbf{o}_\mathrm{u},n,n'}} \\ &= \sum\nolimits_{n=1}^{N}\sum\nolimits_{n'=1}^{N} e^{-j2\pi\left(\frac{\varphi_b}{2\pi} - \left(k_{\tilde{r}_{\mathrm{ru},n,n'}} - k_{r_{\mathrm{ru},n,n'}}\right)\right)} \\ &\overset{(b)}{=} \frac{\sin\left(N\tilde{B}/2\right)\sin\left(N\tilde{C}/2\right)}{\sin\left(\tilde{B}/2\right)\sin\left(\tilde{C}/2\right)} e^{-j\left(\tilde{A} + \frac{N+1}{2}\left(\tilde{B}+\tilde{C}\right)\right)}, \end{aligned} \tag{58}$$

where (b) is obtained by substituting (48) and (55) into (58). Together with (57), we complete the proof.

Appendix C
Proof of Proposition 4

We start from solving the equation $\frac{\sin\left(N\tilde{B}/2\right)}{\sin(\tilde{B}/2)} = N\gamma_B$. Letting $t = \frac{N\tilde{B}}{2}$, we obtain $\frac{\sin t}{N\sin(t/N)} = \gamma_B$. Considering that N is large and assuming that t/N is small, we can approximate the equation as $\frac{\sin t}{t} \approx \gamma_B$. Consequently, we have $\tilde{B} \approx \frac{2}{N}\mathrm{sinc}^{-1}\gamma_B$. Similarly, we have $\tilde{C} \approx \frac{2}{N}\mathrm{sinc}^{-1}\gamma_C$. Recall the definition of $\tilde{B}$ and $\tilde{C}$, we have

$$\frac{k_v\sin\omega - k_{x_u}}{2f(k_{r_{\mathrm{ru}}},k_v,k_u(\omega))} = \frac{1}{N\pi}\mathrm{sinc}^{-1}\gamma_{\tilde{B}} - \frac{k_{x_u}}{2k_{r_{\mathrm{ru}}}}, \tag{59}$$

$$\frac{k_v\cos\omega - k_{y_u}}{2f(k_{r_{\mathrm{ru}}},k_v,k_u(\omega))} = \frac{1}{N\pi}\mathrm{sinc}^{-1}\gamma_{\tilde{C}} - \frac{k_{y_u}}{2k_{r_{\mathrm{ru}}}}. \tag{60}$$

By squaring both sides of (59) and (60), and then adding the two equations together, we obtain

$$\frac{f^2(k_{r_{\mathrm{ru}}},k_v,k_u(\omega)) - k_{z_h}^2}{4f^2(k_{r_{\mathrm{ru}}},k_v,k_u(\omega))} = J_{\mathbf{o}_\mathrm{u}}\left(N,\gamma_B,\gamma_C\right). \tag{61}$$

After some manipulations, we rewrite (61) as

$$f^2\left(k_{r_{\mathrm{ru}}},k_v,k_u(\omega)\right) = \frac{k_{z_h}^2}{1 - 4J_{\mathbf{o}_\mathrm{u}}(N,\gamma_B,\gamma_C)}. \tag{62}$$

Completing the square of $f^2\left(k_{r_{\mathrm{ru}}},k_v,\omega\right)$, we finally obtain that

$$k_v(\omega) = k_u(\omega) + \sqrt{k_{r_{\mathrm{ru}}}^2 + k_u^2(\omega) - \frac{k_{z_h}^2}{1 - 4J_{\mathbf{o}_\mathrm{u}}(N,\gamma_B,\gamma_C)}}. \tag{63}$$

References

[1] H. Tataria, M. Shafi, A. F. Molisch, M. Dohler, H. Sjöland, and F. Tufvesson, "6G wireless systems: Vision, requirements, challenges, insights, and opportunities," *Proceedings of the IEEE*, vol. 109, no. 7, pp. 1166–1199, Jul. 2021.

[2] Q. Wu, S. Zhang, B. Zheng, C. You, and R. Zhang, "Intelligent reflecting surface-aided wireless communications: A tutorial," *IEEE Trans. Commun.*, vol. 69, no. 5, pp. 3313–3351, Jan. 2021.

[3] Liu *et al.*, "Reconfigurable intelligent surfaces: Principles and opportunities," *IEEE Commun. Surveys & Tutorials*, vol. 23, no. 3, pp. 1546–1577, May 2021.

[4] M. D. Renzo, F. H. Danufane, and S. Tretyakov, "Communication models for reconfigurable intelligent surfaces: From surface electromagnetics to wireless networks optimization," *Proceedings of the IEEE*, vol. 110, no. 9, pp. 1164–1209, 2022.

[5] C. Pan and others, "An overview of signal processing techniques for RIS/IRS-Aided wireless systems," *IEEE J. Sel. Top. Signal Process.*, vol. 16, no. 5, pp. 883–917, Aug. 2022.

[6] M. Di Renzo, A. Zappone, M. Debbah, M. S. Alouini, C. Yuen, J. de Rosny, and S. Tretyakov, "Smart radio environments empowered by reconfigurable intelligent surfaces: How it works, state of research, and the road ahead," *IEEE J. Sel. Areas Commun.*, vol. 38, no. 11, pp. 2450–2525, 2020.

[7] L. Dai *et al.*, "Reconfigurable intelligent surface-based wireless communications: Antenna design, prototyping, and experimental results," *IEEE Access*, vol. 8, pp. 45 913–45 923, 2020.

[8] W. Tang *et al.*, "Wireless communications with reconfigurable intelligent surface: Path loss modeling and experimental measurement," *IEEE Trans. Wireless Commun.*, vol. 20, no. 1, pp. 421–439, 2021.

[9] J. Lyu and R. Zhang, "Hybrid active/passive wireless network aided by intelligent reflecting surface: System modeling and performance analysis," *IEEE Trans. Wireless Commun.*, vol. 20, no. 11, pp. 7196–7212, 2021.

[10] A. Kammoun, A. Chaaban, M. Debbah, M.-S. Alouini et al., "Asymptotic max-min SINR analysis of reconfigurable intelligent surface assisted MISO systems," *IEEE Trans. Wireless Commun.*, vol. 19, no. 12, pp. 7748–7764, 2020.

[11] C. Guo, Y. Cui, F. Yang, and L. Ding, "Outage probability analysis and minimization in intelligent reflecting surface-assisted MISO systems," *IEEE Commun. Lett.*, vol. 24, no. 7, pp. 1563–1567, 2020.

[12] Y. Yang, B. Zheng, S. Zhang, and R. Zhang, "Intelligent reflecting surface meets OFDM: Protocol design and rate maximization," *IEEE Trans. Commun.*, vol. 68, no. 7, pp. 4522–4535, 2020.

[13] X. Mu, Y. Liu, L. Guo, J. Lin, and H. V. Poor, "Intelligent reflecting surface enhanced multi-UAV NOMA networks," *IEEE J. Sel. Areas Commun.*, vol. 39, no. 10, pp. 3051–3066, 2021.

[14] Q. Wang, Z. Chen, H. Li, and S. Li, "Joint power and trajectory design for physical-layer secrecy in the UAV-aided mobile relaying system," *IEEE Access*, vol. 6, pp. 62 849–62 855, 2018.

[15] R. J. Williams, E. Carvalho, and T. L. Marzetta, "A communication model for large intelligent surfaces," in *Proc. IEEE ICC Workshops*, 2020, pp. 1–6.

[16] R. Fara, P. Ratajczak, D. Phan-Huy, A. Ourir, M. D. Renzo, and J. D. Rosny, "A prototype of reconfigurable intelligent surface with continuous control of the reflection phase," *IEEE Wireless Commun.*, vol. 29, no. 1, pp. 70–77, 2022.

[17] V. Croisfelt, F. Saggese, I. L-Mayorga, R. Kotaba, G. Gradoni, and P. Popovski, "Random access protocol with channel oracle enabled by a reconfigurable intelligent surface," *IEEE Trans. Wireless Commun.*, pp. 1–1, 2023, early Access.

[18] G. Yang, Y. Liao, Y.-C. Liang, O. Tirkkonen, G. Wang, and X. Zhu, "Reconfigurable intelligent surface empowered device-to-device communication underlaying cellular networks," *IEEE Trans. Commun.*, vol. 69, no. 11, pp. 7790–7805, Aug. 2021.

[19] Y. Chen, B. Ai, H. Zhang, Y. Niu, L. Song, Z. Han, and H. V. Poor, "Reconfigurable intelligent surface assisted device-to-device communications," *IEEE Trans. Wireless Commun.*, vol. 20, no. 5, pp. 2792–2804, Dec. 2021.

[20] H. Chen, H. H. Yang, Q. Tao, and C. Zhong, "Coverage analysis of cell-edge users in reconfigurable intelligent surface-assisted cellular networks," in *Proc. IEEE WCSP*, 2022, pp. 759–763.

[21] D. Shambharkar, S. Dhok, A. Singh, and P. K. Sharma, "Rate-splitting multiple access for RIS-aided cell-edge users with discrete phase-shifts," *IEEE Commun. Lett.*, vol. 26, no. 11, pp. 2581–2585, Aug. 2022.

[22] R. Liu, M. Li, and A. Lee Swindlehurst, "Joint beamforming and reflection design for RIS-assisted ISAC systems," in *Proc. European*

Signal Processing Conference (EUSIPCO), Aug. 2022.
[23] K. Zhong, J. Hu, C. Pan, M. Deng, and J. Fang, "Joint waveform and beamforming design for RIS-Aided ISAC Systems," *IEEE Signal Process. Lett.*, vol. 30, pp. 165–169, Feb. 2023.
[24] H. Luo, R. Liu, M. Li, Y. Liu, and Q. Liu, "Joint beamforming design for RIS-assisted integrated sensing and communication systems," *IEEE Trans. Veh. Techno.*, vol. 71, no. 12, pp. 13 393–13 397, Aug. 2022.
[25] E. Björnson, Ö. Özdogan, and E. G. Larsson, "Intelligent reflecting surface versus decode-and-forward: How large surfaces are needed to beat relaying?" *IEEE Wireless Commun. Lett.*, vol. 9, no. 2, pp. 244–248, 2020.
[26] S. Abeywickrama, R. Zhang, and C. Yuen, "Intelligent reflecting surface: Practical phase shift model and beamforming optimization," in *Proc. IEEE ICC*, 2020, pp. 1–6.
[27] L. Wei *et al.*, "Channel estimation for RIS-empowered multi-user MISO wireless communications," *IEEE Trans. Commun.*, vol. 69, no. 6, pp. 4144–4157, Jun. 2021.
[28] S. Xia *et al.*, "Reconfigurable intelligent surface for massive connectivity: Joint activity detection and channel estimation," *IEEE Trans. Signal Process.*, vol. 69, Oct. 2021.
[29] G. Zhou, C. Pan, H. Ren, P. Popovski, and A. L. Swindlehurst, "Channel estimation for RIS-aided multiuser millimeter-wave systems," *IEEE Trans. Signal Process.*, vol. 70, pp. 1478–1492, Mar. 2022.
[30] Y. Guo, P. Sun, Z. Yuan, C. Huang, Q. Guo, Z. Wang, and C. Yuen, "Efficient channel estimation for RIS-aided MIMO communications with unitary approximate message passing," *IEEE Trans. Wireless Commun.*, vol. 22, no. 2, pp. 1403–1416, Sep. 2023.
[31] L. Mo, X. Lu, J. Yuan, C. Zhang, Z. Wang, and P. Popovski, "Generalized unitary approximate message passing for double linear transformation model," *IEEE Trans. Signal Process.*, vol. 71, pp. 1524–1538, Apr. 2023.
[32] N. S. Perović, M. D. Renzo, and M. F. Flanagan, "Channel capacity optimization using reconfigurable intelligent surfaces in indoor mmWave environments," in *Proc. IEEE ICC*, 2020, pp. 1–7.
[33] X. Tan, Z. Sun, D. Koutsonikolas, and J. M. Jornet, "Enabling indoor mobile millimeter-wave networks based on smart reflect-arrays," in *Proc. IEEE INFOCOM*, 2018, pp. 270–278.
[34] C. Huang, G. C. Alexandropoulos, C. Yuen, and M. Debbah, "Indoor signal focusing with deep learning designed reconfigurable intelligent surfaces," in *Proc. IEEE SPAWC*, 2019, pp. 1–5.
[35] K. Zhi, C. Pan, H. Ren, K. K. Chai, and M. Elkashlan, "Active RIS versus passive RIS: Which is superior with the same power budget?" *IEEE Commun. Lett.*, vol. 26, no. 5, pp. 1150–1154, Mar. 2022.
[36] F. Saggese, F. Chiariotti, K. Kansanen, and P. Popovski, "Efficient URLLC with a reconfigurable intelligent surface and imperfect device tracking," 2022. [Online]. Available: https://arxiv.org/abs/2211.09171
[37] F. Saggese, K. Kansanen, and P. Popovski, "Localization-based OFDM framework for RIS-aided systems," 2023. [Online]. Available: https://arxiv.org/abs/2303.12763
[38] K. Zhi, C. Pan, H. Ren, and K. Wang, "Power scaling law analysis and phase shift optimization of RIS-aided massive MIMO systems with statistical CSI," *IEEE Trans. Commun.*, vol. 70, no. 5, pp. 3558–3574, Mar. 2022.
[39] H. Guo, Y.-C. Liang, and S. Xiao, "Intelligent reflecting surface configuration with historical channel observations," *IEEE Wireless Commun. Lett.*, vol. 9, no. 11, pp. 1821–1824, Jun. 2020.
[40] T. Wu *et al.*, "Exploit high-dimensional RIS information to localization: What is the impact of faulty element?" 2024. [Online]. Available: https://arxiv.org/abs/2403.16529
[41] Z. Peng, Z. Zhang, C. Pan, M. Di Renzo, O. A. Dobre, and J. Wang, "Beamforming optimization for active RIS-aided multiuser communications with hardware impairments," *IEEE Trans. Wireless Commun.*, 2024, early access.
[42] G. R. Maccartney, T. S. Rappaport, S. Sun, and S. Deng, "Indoor office wideband millimeter-wave propagation measurements and channel models at 28 and 73 GHz for ultra-dense 5G wireless networks," *IEEE Access*, vol. 3, pp. 2388–2424, Oct. 2015.
[43] G. Gradoni and M. D. Renzo, "End-to-end mutual coupling aware communication model for reconfigurable intelligent surfaces: An electromagnetic-compliant approach based on mutual impedances," *IEEE Wireless Commun. Lett.*, vol. 10, no. 5, pp. 938–942, 2021.
[44] ELKI Team, "Same-size k-means variation." [Online]. Available: https://elki-project.github.io/tutorial/same-size_k_means

Jide Yuan received his Ph.D. degree in communication and information systems from Southeast University in 2018. From 2018 to 2019, he was with the Institute of Electronics, Communications and Information Technology, Queen's University Belfast. From 2020 to 2022, he was a Research Fellow with the Department of Electronic Systems, Aalborg University. He is currently an Assistant Professor with the School of Electronic and Information Engineering at Soochow University. His current research interests include communication theory, massive MIMO, reconfigurable intelligent surfaces, near-field communications, and integrated sensing and communications.

Ondrej Franek received the Ph.D. degrees in electronics and communication technology from Brno University of Technology in 2006. Since 2005 he has been working as an Assistant and later an Associate Professor with the Department of Electronic Systems, Aalborg University, where he is a member of the Antennas, Propagation and Millimetre-wave Systems section. He is currently on a sabbatical leave working as a senior scientist at Brno University of Technology. His research interests include electromagnetic theory, biological effects of non-ionizing electromagnetic radiation, indoor radio wave propagation, electromagnetic compatibility, ultrawideband propagation, the finite-difference time-domain (FDTD), and most recently reconfigurable intelligent surfaces.

He Fang received her Ph.D. degree in Electrical and Computer Engineering from Western University, Canada, in 2020, and Ph.D. degree in Applied Mathematics from Fujian Normal University, China, in 2018. She is currently a Full Professor with Fujian Normal University, China. Her research interests include intelligent security provision, trust management, machine learning, distributed optimization, and collaboration techniques. She has over 60 peer-reviewed journals and conference papers. She serves as an Associate Editor of China Communications, and a Guest Editor for several journals, including IEEE WIRELESS COMMUNICATIONS and IEEE IoT MAGAZINE. She also served as the Vice-Chair of the Communication/Broadcasting Chapter, IEEE London Section, Canada, from Sep. 2019 to Aug. 2021. She has received several awards, including the Best Paper Award from IEEE GLOBECOM 2023.

Petar Popovski is a Professor at Aalborg University, where he heads the section on Connectivity and a Visiting Excellence Chair at the University of Bremen. He received his Dipl.-Ing and M. Sc. degrees in communication engineering from the University of Sts. Cyril and Methodius in Skopje and the Ph.D. degree from Aalborg University in 2005. He received an ERC Consolidator Grant (2015), the Danish Elite Researcher award (2016), IEEE Fred W. Ellersick prize (2016), IEEE Stephen O. Rice prize (2018), Technical Achievement Award from the IEEE Technical Committee on Smart Grid Communications (2019), the Danish Telecommunication Prize (2020) and Villum Investigator Grant (2021). He was a Member at Large at the Board of Governors in IEEE Communication Society 2019-2021. He is currently an Editor-in-Chief of IEEE JOURNAL ON SELECTED AREAS IN COMMUNICATIONS and a Chair of the IEEE Communication Theory Technical Committee. Prof. Popovski was the General Chair for IEEE SmartGridComm 2018 and IEEE Communication Theory Workshop 2019. His research interests are in the area of wireless communication and communication theory. He authored the book "Wireless Connectivity: An Intuitive and Fundamental Guide".